



HAL
open science

Lacustrine rhythmites from the Mulhouse Basin (Upper Rhine Graben, France): a sedimentary record of increased seasonal climatic contrast and sensitivity of the climate to orbital variations through the Eocene-Oligocene Transition

Emile Simon, Laurent Gindre-Chanu, Cécile Blanchet, Guillaume Dupont-Nivet, Mathieu Martinez, François Guillocheau, Marc Ulrich, Alexis Nutz, Hendrik Vogel, Mathieu Schuster

► To cite this version:

Emile Simon, Laurent Gindre-Chanu, Cécile Blanchet, Guillaume Dupont-Nivet, Mathieu Martinez, et al.. Lacustrine rhythmites from the Mulhouse Basin (Upper Rhine Graben, France): a sedimentary record of increased seasonal climatic contrast and sensitivity of the climate to orbital variations through the Eocene-Oligocene Transition. *Sedimentologica*, In press, 2 (1), 10.57035/journals/sdk.2024.e21.1222 . insu-04485737v1

HAL Id: insu-04485737

<https://insu.hal.science/insu-04485737v1>

Submitted on 1 Mar 2024 (v1), last revised 25 Mar 2024 (v2)

HAL is a multi-disciplinary open access archive for the deposit and dissemination of scientific research documents, whether they are published or not. The documents may come from teaching and research institutions in France or abroad, or from public or private research centers.

L'archive ouverte pluridisciplinaire **HAL**, est destinée au dépôt et à la diffusion de documents scientifiques de niveau recherche, publiés ou non, émanant des établissements d'enseignement et de recherche français ou étrangers, des laboratoires publics ou privés.



Distributed under a Creative Commons Attribution 4.0 International License

1 **Lacustrine rhythmites from the Mulhouse Basin (Upper Rhine Graben, France):**
2 **a sedimentary record of increased seasonal climatic contrast and sensitivity of**
3 **the climate to orbital variations through the Eocene-Oligocene Transition**

4 Emile SIMON^{1*}, Laurent GINDRE-CHANU², Cécile BLANCHET³, Guillaume DUPONT-NIVET^{4,3},
5 Mathieu MARTINEZ⁴, François GUILLOCHEAU⁴, Marc ULRICH¹, Alexis NUTZ⁵, Hendrik VOGEL⁶,
6 Mathieu SCHUSTER^{1*}

7 ¹ Université de Strasbourg, CNRS, Institut Terre et Environnement de Strasbourg, UMR 7063, 5 rue
8 Descartes, Strasbourg F-67084, France

9 ² TERRA GEOSCIENCES, 3 Bis rue des Marmuzots, 21000 Dijon, France

10 ³ Helmholtz Centre Potsdam GFZ, German Research Centre for Geosciences, Telegrafenberg, 14473
11 Potsdam, Germany

12 ⁴ Géosciences Rennes, UMR CNRS 6118, Rennes, 35042 Rennes Cedex, France

13 ⁵ CEREGE, Aix-Marseille Université, CNRS, IRD, Collège de France, INRAE, Aix en Provence,
14 France

15 ⁶ Institute of Geological Sciences & Oeschger Centre for Climate Change Research, University of
16 Bern, Baltzerstrasse 1+3, 3012 Bern, Switzerland

17 *Correspondence concerning this article should be addressed to Emile Simon
18 (emile.simon.geology@gmail.com) and Mathieu Schuster (mschuster@unistra.fr)

19 **Abstract** The Eocene-Oligocene Transition (EOT) marks the passage from Eocene greenhouse to
20 Oligocene icehouse conditions. It holds keys to our understanding of the behavior of climate systems
21 under major pCO₂ shifts. While the environmental impact of the EOT is rather homogenous in oceans,
22 it is much more heterogeneous on continents. Although little to no changes are recorded in some
23 regions, several EOT studies in western Eurasia suggest an increase in seasonal climatic contrast (e.g.,
24 higher amplitude of changes in mean temperature or precipitation), along with a higher sensitivity of the
25 climate to orbital variations. However, these variations remain to be properly documented through
26 changes in sedimentary facies and structures and forcing mechanisms. Here we investigate the
27 depocenter of the Mulhouse Basin (Upper Rhine Graben; URG) revealing a prominent transition from
28 massive mudstones to laminated sediments and varves, alongside the emergence of astronomically-
29 forced mudstone-evaporite alternations. These changes are identified in the distal and proximal parts
30 of the southern URG, where they consist of millimeter-thick mudstone-evaporite couplets and
31 siliciclastic-carbonate couplets. The elemental composition and micro-facies analysis of the laminae
32 show a recurrent depositional pattern consistent with a seasonal depositional process, which suggests
33 that they are varves. We propose that the occurrence of varved sediments, together with the observed
34 orbital cyclicity in the southern URG, reflects an increase in seasonal climatic contrast, and an increase
35 in the sensitivity of climate to orbital variations across the EOT. We show that similar changes were
36 noticed in the Rennes and Bourg-en-Bresse basins, and that of other western Eurasian records for
37 similar climatic conditions. This work emphasizes the potential of high-resolution sedimentary structures
38 to serve as markers of climate change across the EOT.

39 **Lay summary:** The Eocene-Oligocene Transition (EOT) marks the shift from greenhouse to modern
40 icehouse conditions. It is a crucial event to document in order to better understand climate change
41 processes. We studied the lacustrine record of the Mulhouse Basin (Upper Rhine Graben, France) to
42 document the impacts of the EOT on the continental environments of this rift basin. We highlight two
43 major changes in sedimentary deposition patterns. The first is a transition from massive mudstones to
44 finely laminated sediments and varves. The second is the concomitant onset of decameter-thick
45 mudstone-evaporite cycles related to orbital variations. We interpret these changes as induced by an
46 increase in seasonal climatic contrast and in the sensitivity of the climate to orbital variations across
47 the EOT. We show that other continental basins in Eurasia recorded similar sedimentary changes at

48 that time, suggesting a tight link between Eurasian climates and Antarctic icesheets. We highlight the
49 potential of sedimentary structures as sedimentary markers of climate change at the EOT.

50 **Second abstract (French).** La Transition Éocène-Oligocène (TEO) marque le passage des
51 conditions « greenhouse » de l'Éocène aux conditions « Icehouse » de l'Oligocène. Son étude nous
52 permet de mieux comprendre les réponses des systèmes climatiques à des variations majeures de
53 taux de pCO₂. Tandis que l'impact environnemental de la TEO est plutôt homogène dans le domaine
54 océanique, de fortes hétérogénéités sont observées sur les continents. Bien que certaines régions
55 montrent peu de changements, plusieurs études de la TEO suggèrent une augmentation du contraste
56 climatique saisonnier (e.g., plus grande amplitude des changements de la température moyenne et
57 des précipitations), ainsi qu'une plus grande sensibilité du climat aux variations orbitales. Toutefois,
58 ces variations n'étaient pas encore documentées à travers des changements de faciès, de structures
59 sédimentaires, et des mécanismes de forçages. Nous avons étudié ici le dépocentre du bassin de
60 Mulhouse (Fossé Rhéna) qui révèle une transition importante entre des mudstones massives vers
61 des sédiments laminés et des varves, ainsi que l'émergence d'alternances mudstone-évaaporite
62 décamétriques liées aux variations orbitales. Ces structures sont identifiées dans les parties distales
63 et proximales du Fossé Rhéna méridional, où l'on observe des couplets mudstone-évaaporite et des
64 couplets clastique-carbonate millimétriques. La composition élémentaire et l'analyse des micro-faciès
65 des lamines montrent un schéma de dépôt récurrent compatible avec un processus de dépôts
66 saisonnier, ce qui suggère qu'il s'agit de varves. Nous proposons que l'émergence de varves et de
67 cyclicité orbitale observée dans le Fossé Rhéna méridional reflètent une augmentation du contraste
68 climatique saisonnier, et une augmentation de la sensibilité du climat aux variations orbitales à travers
69 la TEO. Nous montrons que des changements similaires existent dans les bassins de Rennes et de
70 Bourge-en-Bresse, et que d'autres enregistrements sédimentaires d'Eurasie témoignent de conditions
71 climatiques semblables. Ce travail souligne le fort potentiel des structures sédimentaires de haute
72 résolution comme marqueurs de changements climatique à travers la TEO.

73

74 *Keywords:* Eocene-Oligocene Transition, Seasonality, Varves, Lake, Upper Rhine Graben

75 1. Introduction

76 The Eocene-Oligocene Transition (EOT) climatic event (~33.9 Ma) is marked by a strong oxygen
77 isotopic shift globally recorded in oceanic benthic foraminifera, interpreted as a combination of a drop
78 in temperature and development of the Antarctic ice-sheet (Zachos et al., 2001; Miller et al., 2020;
79 Hutchinson et al., 2021). Data from deep marine carbon and oxygen stable isotope records suggest
80 that the EOT occurred in several steps. Two major events are the EOT-1 and Oi-1, which are associated
81 with cooling and formation of the Antarctic ice-sheet, respectively. The Oi-1 event resulted in a ca. 70
82 m eustatic sea-level drop (Miller et al., 1991; Zachos et al., 2001; Coxall et al., 2005; Katz et al., 2008;
83 Kennedy et al., 2015; Hutchinson et al., 2021). Two main mechanisms underpinning the EOT have
84 been proposed: (1) the decrease in atmospheric pCO₂, which likely passed a threshold value (DeConto
85 & Pollard, 2003; Pearson et al., 2009; Toumoulin et al., 2022), and/or (2) changes in oceanic gateways
86 (e.g., Atlantic-Arctic, Southern Ocean, and Mesopotamian), which possibly initiated the Antarctic
87 Circumpolar Current (ACC) (Kennett, 1977; Sarkar et al., 2019). Initiation and/or strengthening of the
88 ACC could have thermally isolated Antarctica (thus forcing the glaciation) and enhanced CO₂ drawdown
89 through increasing precipitation on land (silicate weathering) (Straume et al., 2022). In addition, the
90 EOT-1 event corresponds to a period of low summer insolation, which allowed ice sheets to persist
91 during the summer in some places, and eventually spread over the entire Antarctic continent (DeConto
92 & Pollard, 2003; Ladant et al., 2014).

93 The environmental impacts of climate change at the EOT are well-documented in the marine realm,
94 and generally show cooling and increased variability across the globe (Lear et al., 2008; Pearson et al.,
95 2008; Liu et al., 2009; Bohaty et al., 2012; Hutchinson et al., 2021; Toumoulin et al., 2022).
96 Environmental impacts tend to be more heterogenous in continental basins, largely due to the high
97 variability of climate systems affecting continents (Hutchinson et al., 2019; Tardif et al., 2021; Toumoulin
98 et al., 2022). Although various studies report evidence of cooling, aridification, increased seasonal
99 climatic contrast (e.g., decrease in cold month mean temperature and increased aridity; Ivany et al.,
100 2000; Mosbrugger et al., 2005; Dupont-Nivet et al., 2007; Eldrett et al., 2009; Utescher et al., 2015;

101 Page et al., 2019; Hutchinson et al., 2021), and/or biotic turnovers (e.g., Hooker et al., 2004) on
102 continents during the EOT, some do not show any significant climatic changes (Kohn et al., 2015;
103 Zanazzi et al., 2015). These differences potentially provide information relating to the mechanisms and
104 impacts of the EOT, but they remain poorly-documented and quantified.

105 This study focuses on western Eurasia, which is affected by various climate systems during the Eocene
106 and Oligocene. In western Eurasia, the westerly-dominated moisture source may have been modulated
107 by a proto-Atlantic Meridional Overturning Circulation (AMOC; Abelson & Erez, 2017) or affected by
108 tectonically driven reorganization of the Arctic circulation associated with the EOT (Coxall et al., 2018;
109 Straume et al., 2022). Several studies across Eurasia suggest that the decrease in continental
110 temperatures was particularly pronounced in winter, leading to a stronger seasonal temperature
111 contrast that may have driven the well-documented biotic turnovers (e.g., Grande Coupure; Hooker et
112 al., 2004; Mosbrugger et al., 2005; Eldrett et al., 2009; Utescher et al., 2015; Tardif et al., 2021).
113 Furthermore, recent studies have suggested an increase in the sensitivity of climate to orbital variations
114 across the EOT. In the Rennes Basin (France), lacustrine deposits record successive facies shifts
115 before and after the EOT, with strengthening of the eccentricity and precession expressed in the
116 cyclostratigraphical record (Boulila et al., 2021). This can be compared to cyclostratigraphical
117 investigations in north-eastern Tibet, which were affected by westerlies, showing the sedimentary cycles
118 were dominated by eccentricity prior to the EOT, and that a clear change occurred at the Oi-1 event,
119 after which the cycles were paced by a combination of eccentricity, obliquity, and precession (Ao et al.,
120 2020), suggesting a continental-wide increase of the sensitivity of climate to orbital variations. Increased
121 variability and climatic seasonal contrast need to be better established and documented across
122 Eurasian regions to better-assess potential driving mechanisms such as polar amplifications, increased
123 Intertropical Convergence Zone (ICTZ) shifts, proto-AMOC and land-sea interactions in response to
124 continentalization, and aridification (Abelson & Erez, 2017; Tardif et al., 2021).

125 Further documenting the impacts of climate change during the EOT in continental settings of western
126 Eurasia is important as it improves our ability to assess the behavior of climate systems through major
127 atmospheric CO₂ shifts, and to contextualize subsequent environmental changes. An opportunity to
128 study these changes and to investigate climate dynamics through the EOT in a mid-latitude continental
129 setting is provided by the rich sedimentary record of the Upper Rhine Graben (URG) rift system, which
130 is the focus of this study.

131 The URG is composed of several sub-basins that have accumulated continental lacustrine sediments,
132 and epicontinental marine strata during the middle Eocene to late Oligocene (Berger et al., 2005; Simon
133 et al., 2021). The Mulhouse Basin, located in the south of the URG (Figure 1), is characterized by a
134 large accumulation of predominantly lacustrine mudstones and evaporites (e.g., gypsum, anhydrite,
135 halite, sylvite, and carnallite) of the “Zone Salifère Inférieure” (Lower Salt Zone), “Zone Salifère
136 Moyenne” (Middle Salt Zone), and “Zone Salifère Supérieure” (Upper Salt Zone) stratigraphic
137 formations (Blanc-Valleron, 1990; Figure 2). Such evaporitic basins are known to be particularly
138 sensitive to climatic changes (Tanner, 2010). Past investigations in the URG suggested an increase in
139 the seasonal climatic contrast at the base of the “Sel III” (Salt III) stratigraphic unit of the Mulhouse
140 Basin, based largely on palynological changes (Schuler, 1988). It was also suggested that the Eocene-
141 Oligocene boundary is represented at a certain depth within the Sel III, again largely on the basis of
142 biostratigraphic studies and stratigraphic correlations (Grimm et al., 2011). However, large uncertainties
143 remain concerning the chronology, and new constraints are required to improve the chronostratigraphy
144 and characterization of environmental change. So far, most of the information comes from palynological
145 studies that show climate changes across the sedimentary formations (Figure 2; Schuler, 1988).
146 Climatic conditions were subtropical with a short or nonexistent dry season through the “Zone Salifère
147 Inférieure”. Subtropical/mediterranean conditions existed through the “Zone Salifère Moyenne”
148 (suggesting the appearance of a long dry season and thus increased seasonal climatic contrast). A
149 drastic change in climate occurred into a dry and moderately warm mediterranean-type climate grading
150 upwards into further temperate conditions throughout the “Zone Salifère Supérieure”. However,
151 interpretations of the rich sedimentary facies expressed in the records remain rudimentary and have
152 not been directly compared to the climate forcing mechanism attributed to the EOT.

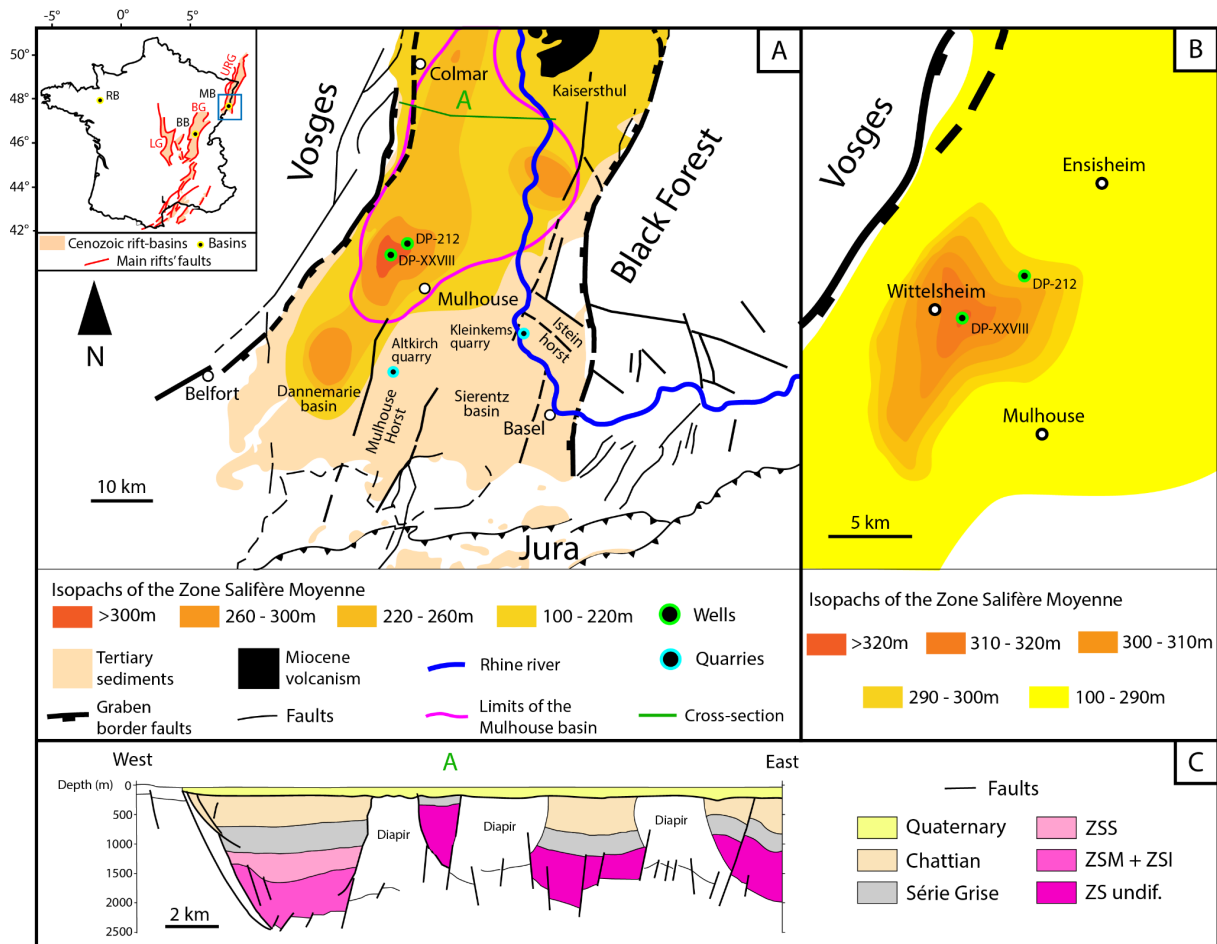
153 Seasonality refers to the annual cycles of temperature and precipitation (Kwiecien et al., 2022) and is
154 a key phenomenon to document in the scope of EOT studies. Seasonality of temperature refers to the
155 amplitude between the temperature maxima and minima, and seasonality of precipitation refers to the
156 amplitude and temporal distribution of precipitation (Kwiecien et al., 2022). While isotopic and

157 palynological investigations (Ivany et al., 2000; Eldrett et al., 2009) and numerical modeling results
158 (Toumoulin et al., 2022) suggest an increase in seasonal climatic contrast at the EOT, marked by a fall
159 in cold month mean temperature and higher aridity, it remains to be documented from specific changes
160 in sedimentary facies and structures, and forcing mechanisms remain unidentified. The URG is
161 therefore an excellent site to investigate the impacts of the EOT as it contains several Eocene-
162 Oligocene lacustrine sequences. Furthermore, prior palynological investigations report an increase in
163 the seasonal climatic contrast at the base of the “Sel III” unit, which is marked by the onset of a long
164 dry season (Schuler, 1988), reinforcing the need for such a study. In this paper, we investigate the
165 sedimentary record of the URG, with the aim of providing insights into potential seasonality contrast
166 changes across the EOT by identifying the development of thinly-bedded cycles and associated
167 sedimentological markers of seasonality.

168 2. Geological Setting

169 Thanks to its rich underground resources (e.g., petroleum, potash, and geothermal brines), the
170 structure, stratigraphy, and sedimentary record of the URG have been widely accessed through seismic
171 imaging, drilling, coring, and borehole petrophysical logging over the past half century (Maikovsky,
172 1941; Sittler, 1965; Schuler, 1988; Blanc-Valleron, 1990; Roussé, 2006). The URG is an intracontinental
173 rift system that contains several middle Eocene to late Oligocene sub-basins (e.g., Mulhouse, Sélestat,
174 and Strasbourg basins), which are separated by structural swells (e.g., Colmar and Erstein). It is part
175 of the European Cenozoic Rift System (ECRS), which extends across ~1,100 km from the
176 Mediterranean to the North Sea. The ECRS formed through the reactivation of Hercynian fracture
177 systems that was induced by the continental collisions of the Alpine and Pyrenean orogens
178 (Schumacher, 2002; Dèzes et al., 2004; Edel et al., 2007). The Tertiary sediments of the URG
179 unconformably overlie the Mesozoic-aged Germanic Basin sediments (e.g., Buntsandstein,
180 Muschelkalk, Keuper, Lias, and Dogger), which cover the crystalline Paleozoic basement (Aichholzer,
181 2019).

182 The Mulhouse Basin is located in the southern part of the URG (Figure 1A), and is delimited by two
183 border faults, with large salt diapirs present in some localities (Figure 1C). The basinal infill is
184 characterized by evaporites (e.g., anhydrite, gypsum, halite, sylvite, and carnallite), which alternate with
185 anhydritic mudstones and carbonates (Blanc-Valleron, 1990). The mudstones primarily consist of
186 marlstones composed of micrite and clay to silt-sized lithogenic grains, sometimes with organic matter
187 (Blanc-Valleron, 1990). The nomenclature of the Mulhouse Basin’s sedimentary fill was first defined by
188 Förster (1911), before being revised by Maikovsky (1941), Courtot et al., (1972), and Blanc-Valleron
189 (1990). The southwestern part of the Mulhouse Basin forms the main depocenter (Figure 1A, B). The
190 “Sel III” unit and “Zone Salifère Supérieure” formations, separated by the “Zone Fossilifère” unit, consist
191 of cyclic meter-thick to decimeter-thick mudstone-evaporite alternations (Figure 2). In the lowermost
192 part of the “Zone Salifère Supérieure”, these alternations have been interpreted as being induced by
193 precession (Blanc-Valleron et al., 1989) based on Sediment Accumulation Rates (SARs) inferred from
194 the finely-laminated mudstones that have been interpreted as varves (Kühn & Roth, 1979).



195

196 **Figure 1:** Localization map and geological structure of the southern Upper Rhine Graben. (A) Study
 197 area and details of the southern Upper Rhine Graben, with the isopachs of the “Zone Salifère Moyenne”,
 198 after Blanc-Valleron (1990), Roussé (2006), and the French geological map. (B) Detailed isopachs of
 199 the “Zone Salifère Moyenne” in the Mulhouse Basin near the DP-XXVIII well, after Blanc-Valleron
 200 (1990). (C) Geological cross-section across the upper part of the Mulhouse Basin, showing the classic
 201 graben structure and occurrence of huge salt diapirs (after Roussé, 2006). URG = Upper Rhine Graben,
 202 MB = Mulhouse Basin, BG = Bresse Graben, BB = Bourg-en-Bresse Basin, LG = Limagnes Graben,
 203 RB = Rennes Basin, ZSS = Zone Salifère Supérieure, ZSM = Zone Salifère Moyenne, ZSI = Zone
 204 Salifère Inférieure, undif. = undifferentiated.

205 The distance between the border faults of the URG reaches approximately 60 km towards the south
 206 across the Mulhouse Basin, and contains relatively complex structures. Two elevated areas known as
 207 the Mulhouse and Istein horsts overhang the rift’s plain. The exposed sediments of the Altkirch Quarry
 208 (Mulhouse horst) range from the “Zone Fossilifère” to the “Haustein” (chronological equivalent of the
 209 “Zone Salifère Supérieure”; Düringer, 1988). The Kleinkems Quarry contains a sedimentary succession
 210 ranging from the Jurassic to the “Zone Fossilifère” (Düringer, 1988). In both quarries, the sedimentary
 211 succession consists of marlstones, limestones, and sandstones, with occurrences of gypsum.
 212 Laminated sediments have been documented earlier by Düringer (1988) from the lowermost geological
 213 section exposed in the Altkirch Quarry and from the uppermost geological section exposed in the
 214 Kleinkems Quarry (“Zone Fossilifère”). Düringer (1988) interpreted some of these laminated sediments
 215 as varves on the basis of their repetitive millimeter-thick alternations of dark- and light-colored laminae,
 216 forming distinct couplets. In the Altkirch Quarry, these deposits correspond to the most distal part of a
 217 prograding axial river delta, and their counterparts in the Kleinkems Quarry are part of a more proximal
 218 segment of a fan delta associated with the eastern border fault (Düringer, 1988).

219 3.1 Material and methods

220 3.1. Rock samples and documentation

221 From 1949 to 1951, a borehole (DP-XXVIII; 1948.6 m) was drilled into Quaternary, Tertiary, and
222 Jurassic sedimentary successions by the Mines Domaniales de Potasse d'Alsace (MDPA) for
223 exploration and production objectives. The isopach maps of the “Zone Salifère Moyenne” (Figure 1)
224 (Blanc-Valleron, 1990) reveal that the DP-XXVIII well captures the depocenter of the Mulhouse Basin,
225 suggesting maximum sedimentary continuity. Core samples from this well (at a scale averaging a
226 sample every few meters) were made accessible by the Musée d'Histoire Naturelle et d'Ethnographie
227 of Colmar for the purposes of the current study (see supplementary files). The preservation of several
228 samples is rather poor, and almost all halite samples are re-precipitated, however most mudstone
229 samples are in good condition. The original detailed lithological description of the DP-XXVIII well by the
230 MDPA was made accessible by the KALIVIE museum (Wittelsheim; MDPA, 1960). The arranged
231 dataset was amalgamated into a sedimentary log of the well (see supplementary files). In addition,
232 laminated rock samples were collected from the “Zone Fossilifère” unit exposed in both the Altkirch and
233 Kleinkems quarries (Figure 1A).

234 3.2. Sediment macro- and micro-facies analysis

235 Micro-facies descriptions were performed on both thin and thick sections from selected and suitable
236 samples of the DP-XXVIII well, and the Altkirch and Kleinkems quarries. Both macro- and micro-facies
237 descriptions, as well as thin and thick section photographs were realized using a Leica M205 C stereo
238 microscope. A total of 203 core samples have been investigated and their positions in the sedimentary
239 log of the well are shown in the supplementary file (Figure S1).

240 3.3. Micro X-Ray fluorescence scanning

241 Micro X-Ray Fluorescence (μ -XRF) analyses were performed on thin and thick sections using a Bruker
242 M4 Tornado spectrometer at the Institut Terre & Environnement of Strasbourg. The maximum resolution
243 of 20 μ m was used in order to achieve the best representative elemental counts for each lamina. The
244 spectrometer settings were set on a voltage of 50 kV, ampere ratings of 400 μ A, and the analyses were
245 performed under vacuum conditions (2 mbar). We selected a set of representative elements to
246 determine the relative changes in detrital input (aluminum, silica potassium, titanium, iron – Al, Si, K,
247 Ti, Fe) and chemogenic or diagenetic deposition (calcium, strontium, sulfur – Ca, Sr, S) (Boès et al.,
248 2011; Davies et al., 2015). Elemental contents are reported as log-ratios in order to avoid closed-sum
249 constraints (Weltje et al., 2015).

250 3.4. Scanning electron microscope

251 Scanning Electron Microscope (SEM) images and local chemical analyses were performed on a thin
252 section and on a rock sample from the DP-XXVIII well to document the chemistry and microstructure of
253 minerals using a VEGA TESCAN machine.

254 3.5. Spectral analysis

255 Spectral analysis was performed on the Gamma-Ray (GR) series from the “Sel V” unit of the DP-212
256 well to test the hypothesis of orbital forcing of the meter-thick to decameter-thick mudstone-evaporite
257 alternations. The GR was measured by the MDPA through Schlumberger electrical logging and records
258 the natural radioactivity of the sedimentary record. The GR series was interpolated, linearly detrended,
259 and normalized using Acycle's “normalize” function (z-scoring, Li et al., 2019). Sedimentary cycles and
260 their evolution were studied using the Multi-Taper Method applying 2π -tapers with red-noise modeling
261 (2π -MTM analysis; robust AR(1) test) to detect statistically significant sedimentary cycles (Thomson,
262 1982; Mann & Lees, 1996), the Evolutive Fast Fourier Transform (EFFT) to document the evolution of
263 sedimentary cycles through depth (Weedon, 2003), and Taner band-pass filters to isolate specific
264 broadbands (Taner, 2000). These methods were performed using the Acycle software (v2.3.1; Li et al.,
265 2019). The classical AR(1) test was also performed (Priestley, 1981).

266 4. Results

267 4.1. DP-XXVIII well

268 4.1.1. Synthetic sedimentary log

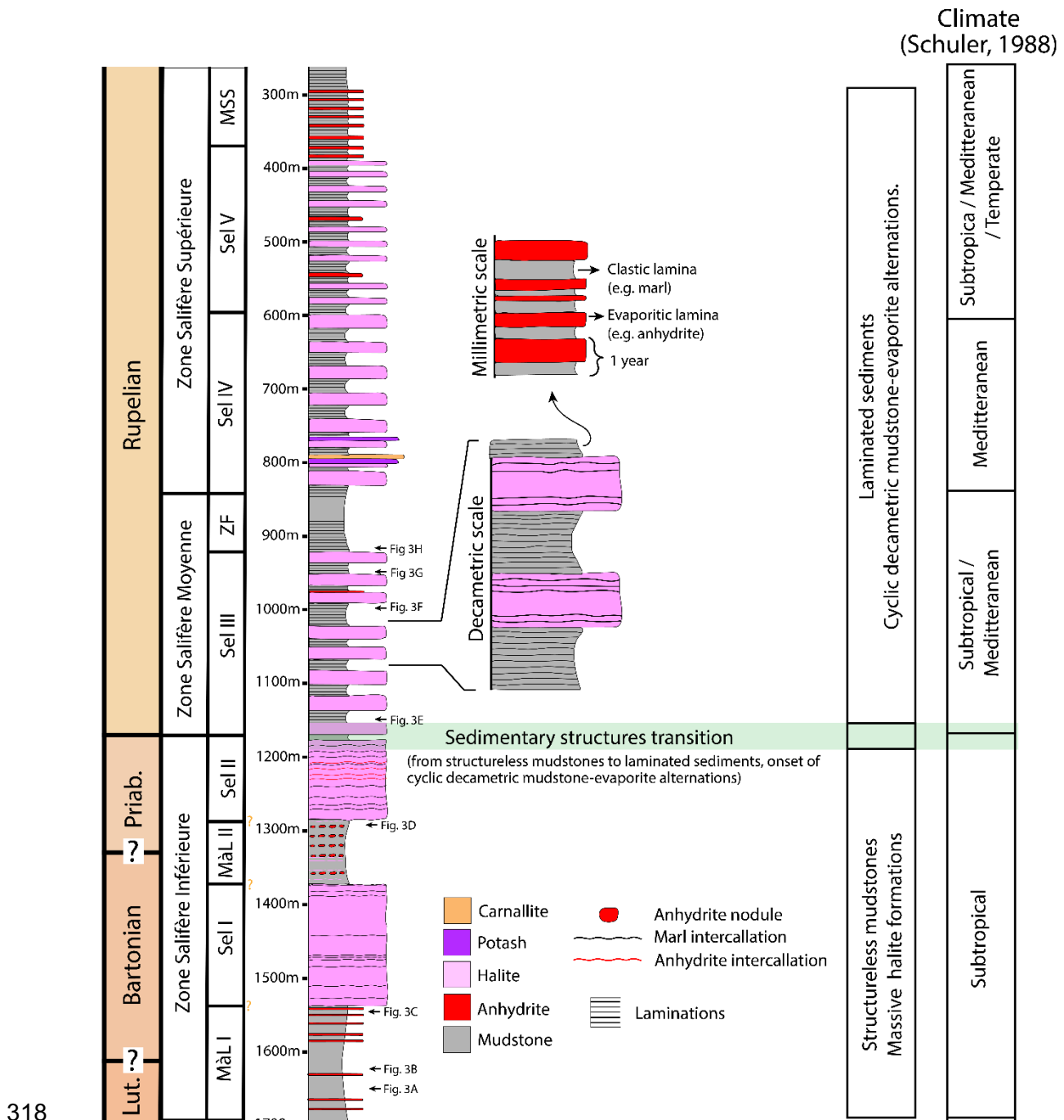
269 The detailed sedimentary log of the DP-XXVIII well (see supplementary files) was produced based on
270 the written description of the sedimentary successions made by the MDPA in the mid-20th century
271 (MDPA, 1960), which we then synthesized (Figure 2). Here, we focus on the three zones as defined by
272 Blanc-Valleron (1990) to investigate sedimentary changes across the EOT.

273 The “Zone Salifère Inférieure” is divided into four units (from base to top): the “Marnes à Limnées I”
274 (Limnea Marls I) unit (thickness: 155 m) consists of massive mudstones alternating with centimeter to
275 meter thick, bedded to nodular anhydrite layers. The “Sel I” (Salt I) unit (thickness: 165 m) is a massive
276 halite formation with rare intercalations of centimeter-thick mudstone and anhydrite layers. The halite is
277 described as made up of centimeter-thick crystals forming chevrons (MDPA, 1960), which could
278 correspond to bottom nucleated beds of coarse growth-aligned crystals at the sediment/water interface.
279 The lithology of the “Marnes à Limnées II” (Limnea Marls II) unit (thickness: 84 m) is similar to the
280 “Marnes à Limnées I”, followed by the “Sel II” (Salt II) unit (thickness: 117 m), which has a similar
281 lithology as the “Sel I” unit, contains substantially more intercalations of centimeter-thick to meter-thick
282 mudstone and anhydrite beds.

283 The “Zone Salifère Moyenne” comprises two units (from base to top). The “Sel III” unit (thickness: 249
284 m) consists of cyclic decimeter-thick alternations of laminated mudstones and massive halite beds (their
285 average thickness is ~12.6 m). The laminated mudstones of this unit are often described as made up
286 of millimeter-thick laminae (MDPA, 1960). The overlying “Zone Fossifère” (Fossiliferous Zone) unit
287 (thickness: 80 m) is a thick mudstone formation attributed to a transgression event that flooded the
288 whole URG during the early Rupelian (Berger et al., 2005; Pirkenseer et al., 2010) and consists of
289 laminated mudstones with occasional dolomite and anhydrite layers.

290 The “Zone Salifère Supérieure” is composed of three units (from base to top). The “Sel IV” (Salt IV) unit
291 (thickness: ~246 m) is made of cyclic decimeter-thick mudstone-halite alternations (average thickness
292 of ~12.4 m). The mudstone beds of these alternations are mostly laminated. Two meter-thick intervals
293 of centimeter-thick halite and sylvite alternations (commonly draped by anhydritic marlstones and
294 dolomitic carbonates), with occasionally interbedded centimeter-thick laminated boundstones, are
295 identified at the bottom of the formation. A 1.2 m thick carnallite bed is located at the top of the lower
296 potash seam. The “Sel V” unit (thickness: ~227 m) is made of cyclic meter-thick alternations of halite
297 (or anhydrite) and mudstone beds, which average ~8.3 m in thickness. The following “Marnes sans Sel”
298 (Salt-free Marls) unit (thickness: ~106 m) consists of cyclic meter-thick mudstone-anhydrite alternations
299 (with an average thickness of ~5.6 m). The mudstone beds of these alternations appear mostly
300 laminated, yet the upper ~45 m is composed of a thick mudstone section without any observable
301 sedimentary alternations. Overall, the “Zone Salifère Supérieure” is characterized by its cyclic meter-
302 thick to decimeter-thick mudstone-evaporite alternations, where the mudstones are mostly laminated,
303 and by the presence of two potash seams in its lowermost part.

304 Across the three formations, the mudstones can be divided into two main groups according to the
305 absence or presence of sedimentary structures: (1) massive and (2) laminated mudstones. Massive
306 mudstones are common in the “Zone Salifère Inférieure”, where very few laminated mudstones have
307 been described (MDPA, 1960). In the lowermost “Zone Salifère Moyenne”, a clear facies change occurs
308 with the appearance of laminated mudstones that make-up most of the mudstones up to the top of the
309 “Zone Salifère Supérieure”. The seemingly cyclic decimeter-thick mudstone-evaporite alternations
310 appear at the same depth as the finely-laminated mudstones and remain a predominant feature up to
311 the uppermost “Zone Salifère Supérieure”. However, evaporites are scarce in the “Zone Fossifère”,
312 even though laminated mudstones remain prevalent. To sum up, the study of the original description of
313 the DP-XXVIII well (MDPA, 1960) reveals that both the millimeter-thick laminae and the recurrent meter-
314 thick to decimeter-thick mudstone-evaporite alternations appear at the bottom of the “Sel III” (depth:
315 1158 m) and are found up to the uppermost part of the “Zone Salifère Supérieure” (depth: 312 m). The
316 mudstone-evaporite alternations become thinner upward in the section, from ~12.6 m in the “Sel III” to
317 ~5.6 m in the “Marnes sans Sel”, suggesting a gradual decrease in SARs.



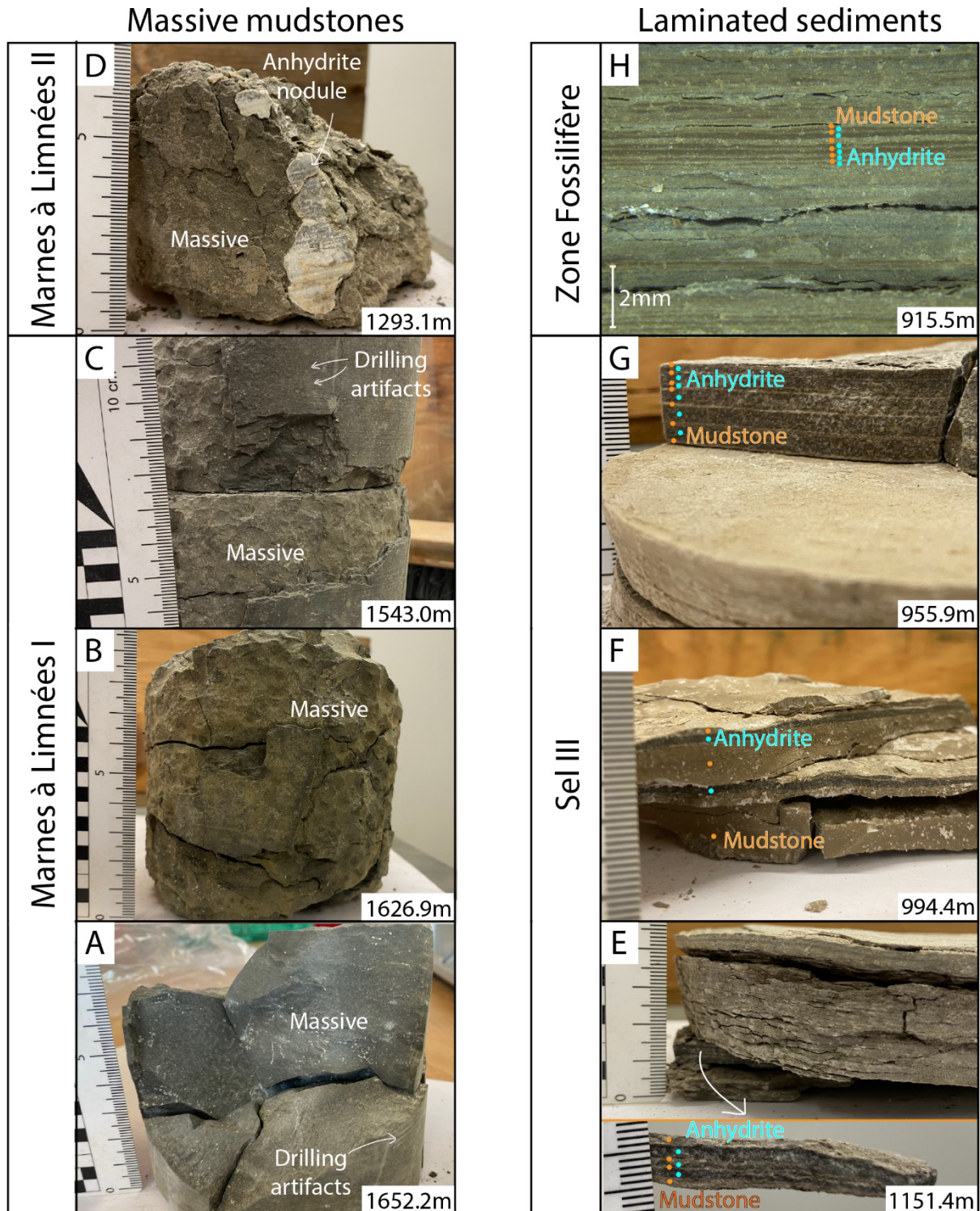
318

319 **Figure 2:** Synthetic log of the sedimentary succession of the Mulhouse Basin's formations through a
 320 segment of the DP-XXVIII well, with the paleoclimatic observations inferred from palynology (Schuler,
 321 1988). The chronostratigraphy is based after Grimm et al. (2011) and Châteauneuf & Ménillet (2014),
 322 and the Eocene-Oligocene boundary is placed according to the correlations presented in this paper.
 323 The thickness of the mudstone-evaporite alternations of the "Sel III" and "Zone Salifère Supérieure" are
 324 exaggerated. MâL I = Marnes à Limnées I, MâL II = Marnes à Limnées II, MSS = Marnes sans Sel.

325 4.1.2. Macro-facies of the core samples

326 The three main lithologies represented in the DP-XXVIII core are mudstone, halite, and anhydrite.
 327 Macro-facies observations of the mudstones are in accordance with the available description (MDPA,
 328 1960; Figure 3). The massive mudstones are predominant in the "Zone Salifère Inférieure", whereas
 329 the laminated mudstones are predominant in the "Zone Salifère Moyenne". However, a few laminated
 330 samples are present in the "Sel II" unit. The laminated mudstones consist of millimeter-thick laminae,

331 several of which are made of couplets of dark- and light-colored laminae, especially moving upward
 332 from the base of the “Sel III” unit. At the macroscopic scale, the dark-colored laminae are primarily
 333 composed of anhydrite, while the light-colored laminae are mainly composed of siliciclastic mud (Figure
 334 3E-H). While some are very finely laminated (e.g., Figure 3E, G), others exhibit thicker layers (e.g.,
 335 Figure 3G). At the microscopic (thin section) scale, the color pattern of these laminae is the opposite,
 336 with anhydrite laminae being light-colored and mudstone laminae being dark-colored (Figure 4).



337

338 **Figure 3:** Macro-photographs of core samples from the DP-XXVIII well. (A, B, C, D) Massive mudstones
 339 with conchoidal fractures. Coring artifacts from the drill machine are not to be mistaken with laminations.

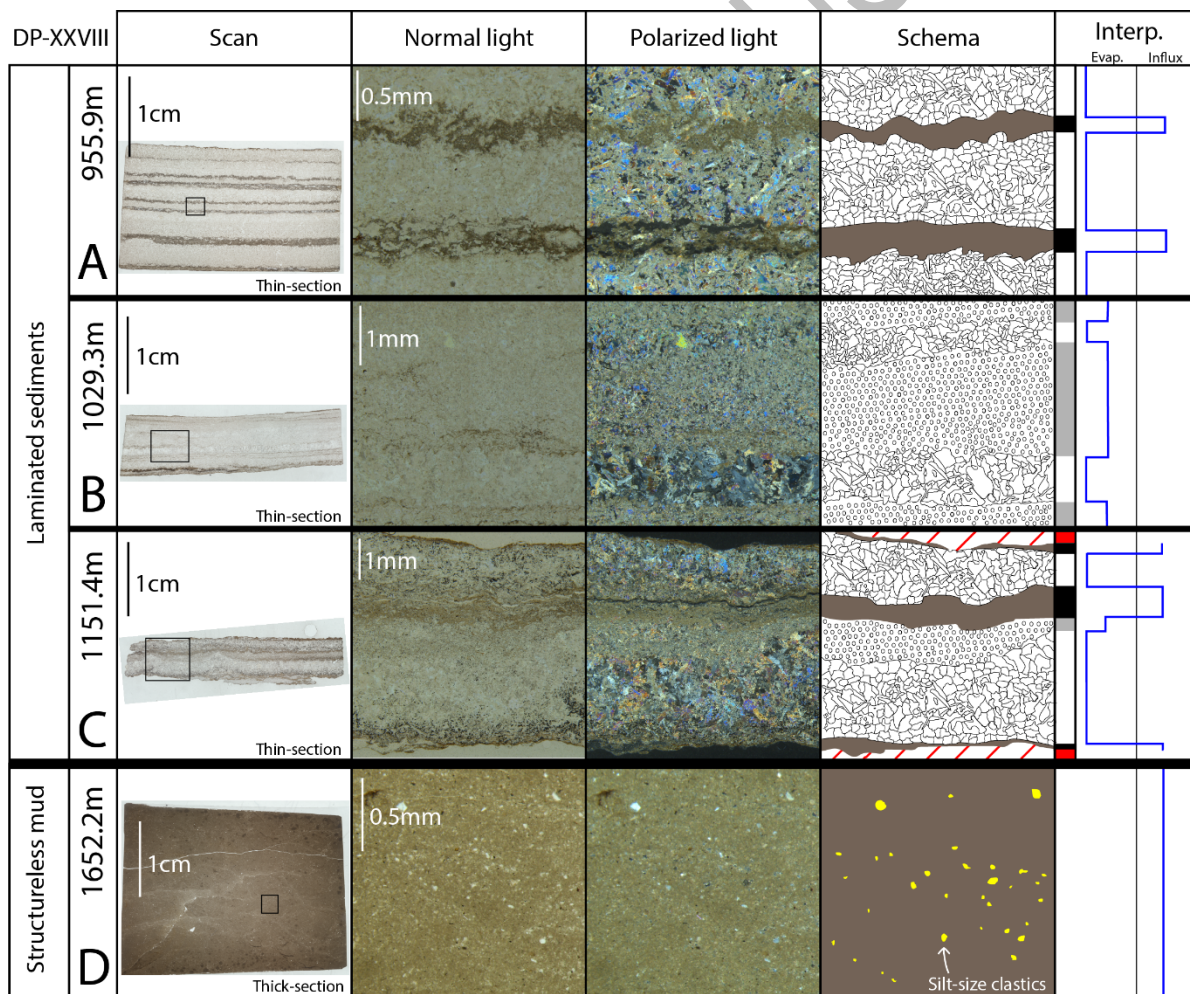
340 (E, F, G, H) Laminae consisting of mudstone (light-colored laminae) and anhydrite (dark-colored
 341 laminae) couplets.

342 The halite core samples have been impacted by recrystallization, preventing proper identification of the
 343 depositional environment. The anhydrite either forms centimeter-thick elongated to sub-rounded nodule
 344 beds, with vestigial bottom-growth structures encompassing marlstone, or layers.

345 **4.2. Laminated sediments of the southern Upper Rhine Graben**

346 **4.2.1. Depocenter (DP-XXVIII well)**

347 In the “Zone Salifère Moyenne”, 61 out of 68 mudstone samples are laminated (see supplementary
 348 files). Observation of the samples under the microscope reveals repetitive couplets and triplets of dark-
 349 and light-colored laminae (Figure 4). The 955.9 m sample consists of repetitive couplets of anhydrite
 350 pseudomorphs derived from bottom-growth gypsum (light-colored laminae) and marlstones (dark-
 351 colored laminae). The 1151.4 m sample contains an additional fine-grained (~30 µm) anhydrite lamina
 352 (cumulates). Dark-colored laminae contain homogenous and massive clay-sized sediments. Some of
 353 the laminae are black, suggesting an enrichment in organic matter as indicated by the SEM
 354 measurements. In the case of the 1029.3 m sample, the sediments are typified by two couplets of
 355 anhydrite pseudomorph laminae, overlain by of discontinuous draping clay, without significant
 356 dissolution surfaces. Typically, gypsum pseudomorphs form as bottom-nucleated crystals that grown
 357 on the lake floor when brine is saturated with respect to sulfates (Warren, 2016).



Anhydrite pseudomorphs after bottom-growth gypsum



Anhydrite cumulates

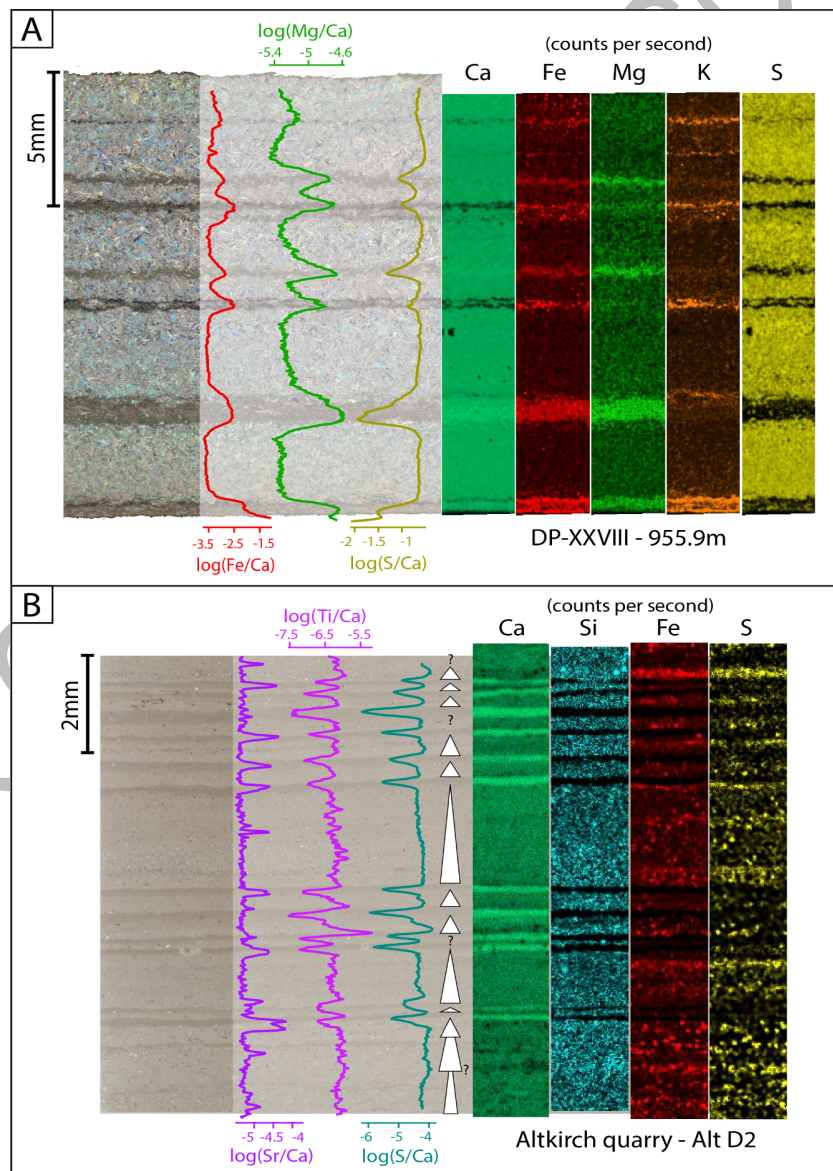


Mudstone

358

359 **Figure 4:** Thin sections of laminated sediments, and thick section of a massive mudstone, from the DP-
 360 XXVIII well. A) Laminated sediments made of couplets of mudstones and anhydrite pseudomorphs after
 361 bottom-growth gypsum (955.9 m). B) Laminated sediments made of couplets of anhydrite
 362 pseudomorphs after bottom-growth gypsum and anhydrite cumulates with some very thin mudstone
 363 drapes (1029.3 m). C) Laminated sediments made of couplets of mudstone, anhydrite pseudomorphs
 364 overlying bottom-growth gypsum, and anhydrite crystals (1151.4 m). D) Massive mudstone consisting
 365 of silt-sized clastic grains in a micrite matrix (1652.2 m).

366 The elemental geochemistry analysis of the 955.9 m sample shows that the light-colored laminae are rich
 367 in Ca and S, which track the presence of anhydrite, which is also inferred from microfacies
 368 observations (Figure 5A). The dark-colored laminae are enriched in Fe, Mg, and K, which indicates they
 369 are primarily composed of detrital siliciclastic minerals (clay). The dark-colored laminae are enriched in
 370 Mg (high Mg/Ca ratios) and can therefore contain dolomite ($\{Ca,Mg\}CO_3$) which amount might depend
 371 on the presence of Ca (see element maps, Figure 5A). The S content is generally low in dark-colored
 372 laminae (low S/Ca ratios), which confirms the absence of anhydrite, but enrichments of S are
 373 occasionally observed. This can possibly be attributed to the presence of diagenetic processes that
 374 induce pyrite precipitation (FeS_2) (e.g., the third mudstone laminae starting from the bottom, Figure 5A).
 375 Similar elemental compositions were found for the samples at 1029.3 m and 1151.4 m depth (see
 376 supplementary files), which suggest similar genesis of the sediments as the sample at a depth of 955.9
 377 m.

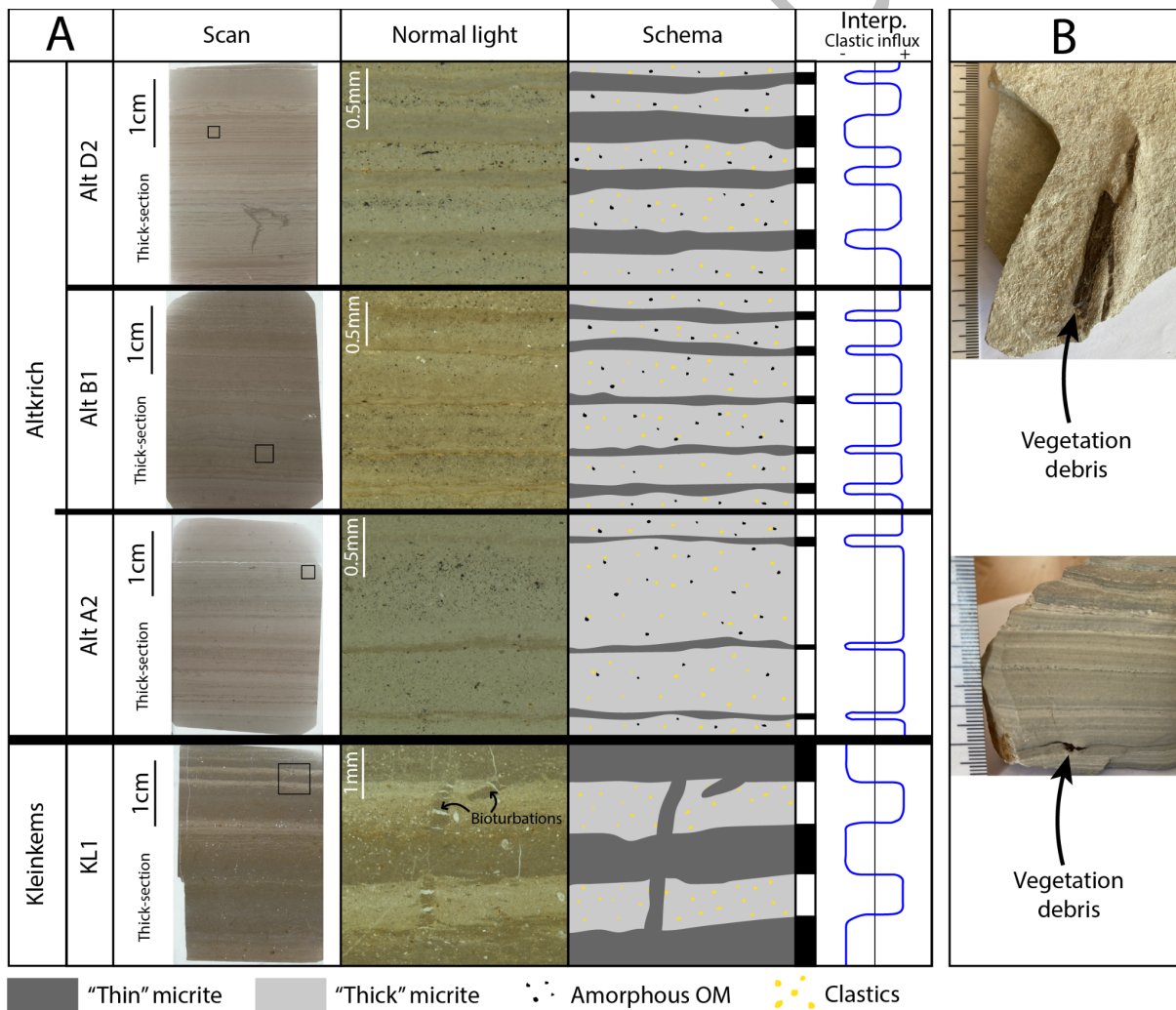


378

379 **Figure 5:** μ -XRF analyses consisting of logarithms of specific elemental ratios and elemental mappings
 380 of the DP-XXVIII well sample, at depth 955.9 m, and of the Alt-D2 sample from the Altkirch Quarry. In
 381 the case of elemental mappings, black represents no counts per second, while the colors represent
 382 higher counts per seconds based on the intensity. The white triangles represent fining-up sequences.
 383 (A) (DP-XXVIII - 955.9 m) The μ -XRF analyses show that the light-colored laminae are anhydrite (rich
 384 in Ca and S) and that the dark-colored laminae range from marl to dolomite due to their varying
 385 intensities of Ca and Mg. Furthermore, the elemental mappings show an enrichment in lithogenic
 386 elements (e.g., Fe, K) in the dark-colored laminae, suggesting their detrital nature. (B) (Altkirch Quarry
 387 - Alt D2) The μ -XRF analyses show that the dark-colored laminae are rich in Ca, enriched in Sr, and
 388 completely devoid of lithogenic elements, suggesting an evaporitic nature. Inversely, the light-colored
 389 laminae are enriched in lithogenic elements (e.g., Si, Ti, Fe), which suggests a detrital nature, further
 390 demonstrated by fining-up sequences.

391 **4.2.2. Altkirch Quarry**

392 The laminated sediments from the lowermost part of the Altkirch Quarry (“Zone Fossilifère”) were first
 393 described as varves based on the repetitive nature of their dark- and light-colored laminae (Düringer,
 394 1988; Figure 6). The dark-colored laminae are homogenous, have a constant thickness, and consist of
 395 very fine micrite crystals (<1 μ m). The light-colored laminae (0.15 – 2 mm thick) are composed of larger
 396 micrite crystals (~2 μ m) and contain clastic grains, along with amorphous organic matter (Figure 6A).
 397 The Altkirch Quarry is known for its rich diversity of macrofossil taxons (e.g., fish, insects, and mollusks;
 398 Gaudant & Burkhardt, 1984), thus a certain amount of the organic content could also be autochthonous.



399 **Figure 6:** (A) Thick sections of laminated sediments from the Altkirch and Kleinkems quarries (“Zone
 400 Fossilifère”). (Alt D2, Alt B-1, and Alt-A2) Laminated sediments made of couplets of thin micrite crystals
 401

402 (dark-colored laminae) and thicker micrite crystals, amorphous organic matter, and detrital grains (light-
403 colored laminae). (KL1) Laminated sediments similar to those from the Altkirch Quarry, but without
404 amorphous organic matter, and with shells across the laminae. (B) Macro-photographs of laminated
405 sediments from the Altkirch Quarry containing macroscopic vegetation debris.

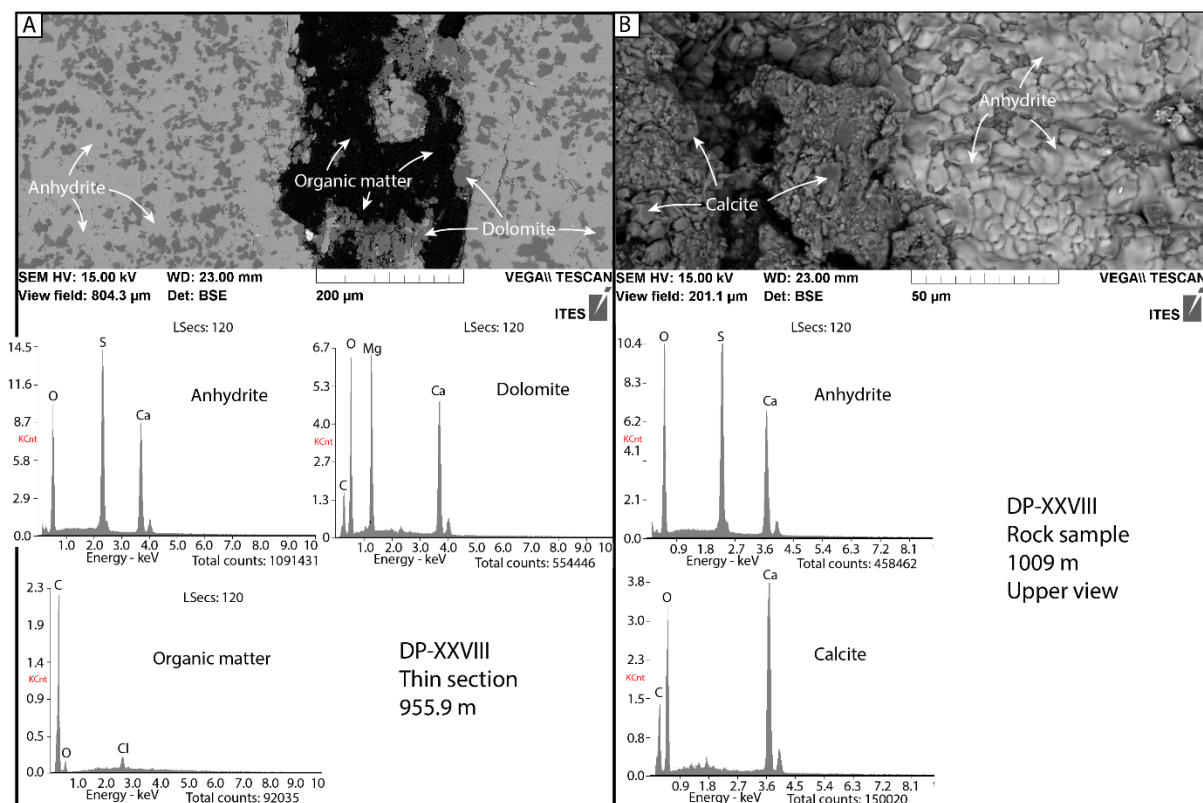
406 Elemental analyses of the Altkirch laminated sediments (Alt D2 sample, Figure 5B) show that the dark-
407 colored laminae are enriched in Ca and Sr, while the Si, Ti, Fe, S, and K values are higher in the light-
408 colored laminae (Figure 5B). Several dark-colored layers also contain higher concentrations of Sr
409 (higher Sr/Ca ratios), which potentially indicates the presence of Sr-enriched carbonates, such as
410 aragonite or strontianite. Dark-colored layers are devoid of detrital material (low Si/Ca and Ti/Ca ratios,
411 absence of Si and Fe in element maps), which suggests that the thin micrite crystals of the latter are
412 chemogenic (evaporitic) rather than detrital. In light-colored layers, high levels of lithogenic elements
413 (e.g., Si, Fe, and Ti) track the input of clastic material (e.g., quartz, and feldspars) identified in the micro-
414 facies analysis. The detrital-rich light-colored laminae show distinct fining-upward sequences (Figure
415 5B), which is evidenced by decreasing log-ratio profiles of Si/Ca and Ti/Ca and decreasing grain-sizes
416 observable on the elemental map of Si. The enrichment in both Fe and S in light-colored laminae
417 suggests the presence of iron sulfides (e.g., pyrite). The clastic grains in the light-colored layers are
418 encased in a micrite matrix (cement). Comparable results were found for the Alt A2 and Alt B1 samples
419 (see Data Availability), which suggest that their laminae are similar in nature to those of the Alt D2
420 sample.

421 4.2.3. Kleinkems Quarry

422 The laminated sample from the Kleinkems Quarry contains several successions of dark- and light-
423 colored calcareous laminae (Figure 6). The dark-colored laminae are comparable to those from the
424 Altkirch Quarry and are composed of homogeneous bioclastic fine-grained micrite, with randomly
425 distributed shells. The light-colored laminae, similarly to those from Altkirch Quarry, contain a significant
426 amount of clastic grains, but no amorphous organic matter. The μ -XRF analysis of the KL1 sample
427 shows similar elemental distribution as in the samples from the Altkirch Quarry (see supplementary
428 files). However, the dark-colored Ca-rich laminae also contains some detrital material, as indicated by
429 the presence of a few lithogenic grains.

430 4.3. Scanning Electron Microscope

431 SEM images and localized chemical analyses of a part of the 955.9 m thin section shows the presence
432 of anhydrite (light gray), dolomite (dark gray), and organic matter (black) (Figure 7A). Small dolomite
433 patches are encased in the anhydrite. The image of the sample at depth 1009 m shows the presence
434 of anhydrite (light gray) and calcite (dark gray) arranged in layers (upper view) (Figure 7B). The
435 anhydrite is characterized by high counts of Ca, S, and O; the dolomite by high counts in Ca, Mg, O,
436 and C; the calcite by high counts in Ca, O, and C, and the organic matter by high counts in C.

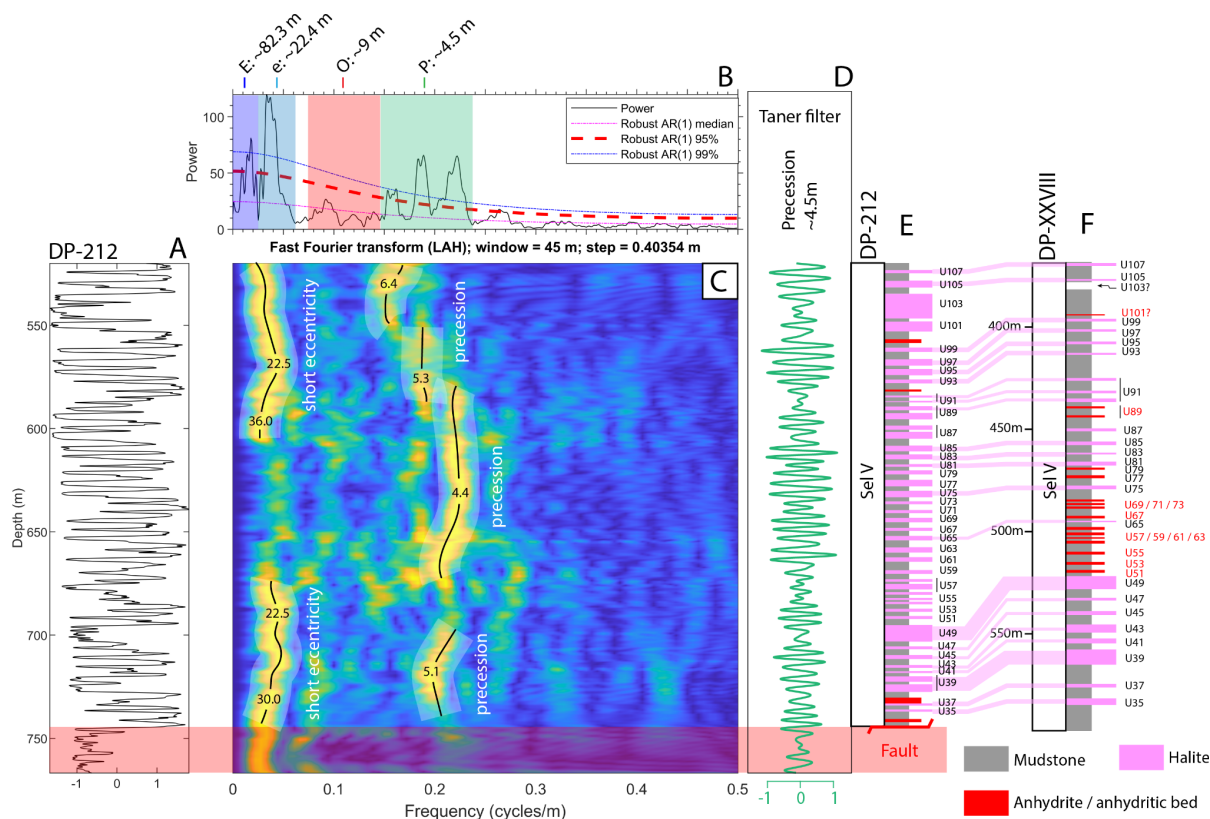


437

438 **Figure 7:** SEM images and localized chemical analyses of a part of the (A) thin section at 955.9 m
 439 depth and (B) sample at 1009 m depth.

440 4.4. Spectral analysis

441 The 2π-MTM analysis results of the detrended GR series (Figure 8A) of the “Sel V” unit from the DP-
 442 212 well reveals statistically significant frequency broadbands related to sedimentary cycles, with
 443 average thicknesses of 82.3 m, 22.4 m, and 4.5 m (>99% confidence level), and 9 m (> median
 444 confidence level) (Figure 8B). The broadband related to the ~4.5 m thick sedimentary cycle shows three
 445 distinct peaks. The EFFT shows that the ~22.4 m and the ~4.5 m cycle are prominent throughout the
 446 sedimentary record (Figure 8C). The Taner filter of the ~4.5 m cycle is in-phase with the large majority
 447 of the mudstone-evaporite alternations (Figure 8D, E). The classical AR(1) test shows that almost the
 448 whole signal is above the 99.9% confidence level, and that the same frequency peaks appear with the
 449 highest amplitudes, except for the ~82.3 m cycle (see supplementary files).



450

451 **Figure 8:** Spectral analysis results of the “Sel V” unit of the DP-212 well (“Zone Salifère Supérieure”).
 452 (A) Linearly detrended gamma-ray series (DP-212). (B) 2π -multitaper spectrum with linearly fitted red-
 453 noise modelling. E = long eccentricity, e = short eccentricity, O = obliquity, P = precession. (C) EFFT
 454 with a sliding window of 45 m and a step of 0.40354 m. (D) Taner filter of the precession (P; 0.1459 –
 455 0.2998 cycles/m) cycles. (E) Sedimentary log of the DP-212 well (“Sel V”). (F) The equivalent
 456 sedimentary log of the DP-XXVIII well (“Sel V”). The “U” followed by numbers are the name of each
 457 halite bed as initially established by the MDPA (Blanc-Valleron, 1990).

458 5. Interpretation and discussion

459 To achieve the goals of this study, we interpret and discuss in the following sections the results
 460 presented above to:

- 461
- 462 • estimate whether the observed laminae represent an annually deposited cycle (varves) and
 - 463 if they can thus be used as markers of seasonality;
 - 464 • discern the possible mechanisms behind the cyclic sedimentation pattern of the laminae and
 - 465 decameter-thick mudstone-evaporite alternations, with implication for better understanding
 - 466 past environmental changes;
 - 467 • and to place the interpretation of this study in a wider regional scale and to discuss the
 - 468 implications for climatic changes across the EOT.

468 5.1. Laminated sediments and varves: nature and depositional processes

469 Distinguishing varves from non-annual laminated sediments is challenging for sedimentary archives
 470 beyond the radiometric time range. While the annual nature of varves in modern and recent lacustrine
 471 and marine environments can be determined using various means (Zolitschka et al., 2015), it can only
 472 be hypothesized in older geological (deep-time) records, by interpreting and comparing of
 473 petrographical and geochemical data with their modern and recent counterparts (Wilson & Bogen, 1994;
 474 Mingram, 1998). For the southern URG, we use the sedimentary records of the Dead Sea, which contain
 475 extensive evaporite deposits (Ben Dor et al., 2019), and of Chatyr Kol Lake (Kalanke et al., 2020) as

476 sedimentary analogues, which allow us to propose conceptual models for reconstructing depositional
477 processes.

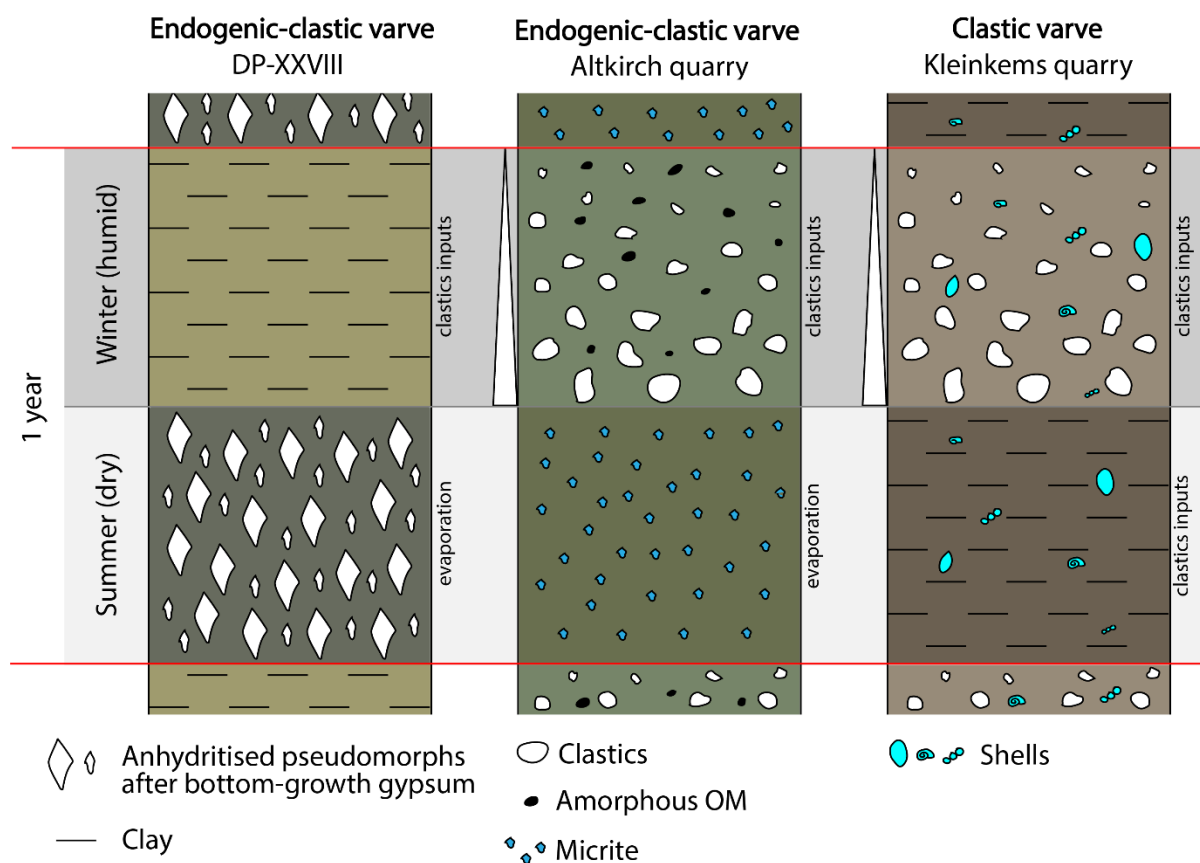
478 **5.1.1. Distinguishing varves from laminated sediments**

479 Lacustrine sediments, such as laminated sediments and varves, can be categorized as clastic, biogenic,
480 or endogenic (Brauer et al., 2009; Zolitschka et al., 2015). Varves are a particular type of laminated
481 sediments, which are defined as sedimentary layers of distinct composition, occurring as repetitive
482 patterns that represent annual cycles (Zolitschka et al., 2015). The identification of varves is a strong
483 indicator of local climatic seasonality. Clastic varves are formed when suspended sediment carried by
484 seasonal runoff enters a lake with a stratified water body (Sturm, 1979). They are typically made of
485 laminae with different grain sizes that results from distinct seasonal runoff regimes. Biogenic varves are
486 formed when seasonality induces changes in the organic productivity of a lake, resulting in the
487 deposition of distinct biogenic laminae (e.g., algal blooms, diatom blooms; Lake Tiefer, Germany;
488 Dräger et al., 2017). Endogenic varves, which are often evaporitic, occur when the solubility product of
489 a mineral compound (e.g., anhydrite, halite, and aragonite) is exceeded due to seasonal fluctuations of
490 evaporation and/or precipitation (e.g., the Dead Sea; Ben Dor et al., 2019). It is rare that varves are
491 either purely clastic, biogenic, or endogenic (Zolitschka et al., 2015). The Varves Database provides an
492 overview of many varve records and of their characteristics (Ojala et al., 2012). It should be noted that
493 the presence of laminated sediments and varves indicates that the depositional environment prevented
494 the development of benthic life and bioturbation. It is however beyond the scope of our study to
495 determine whether it has been the lack of oxygen or a specific water chemistry (e.g., hypersaline
496 waters), or a combination of the two that have rendered the lake floor uninhabitable.

497 **5.1.2. Interpretation of the fine laminations as varves and conceptual depositional model**

498 **5.1.2.1. Depocenter (DP-XXVIII well)**

499 The samples from the DP-XXVIII core display clear couplets of mudstone and anhydrite pseudomorphs
500 after bottom-growth gypsum, with no dissolution surfaces (Figure 4, Figure 5A). We propose that the
501 evaporites were formed through evaporation-driven brine saturation during the dry season, and that the
502 intercalated mudstone layers (sometimes rich in organic matter) were formed due to enhanced fluvial
503 runoff during the wet season (Figure 9). This interpretation is supported by the elemental profiles that
504 clearly distinguish between anhydritic laminae (enriched in Ca and S) and detrital mudstone laminae
505 (enriched in the lithogenic elements Fe and K) (Figure 5A). According to the palynological investigations
506 and taking into account the mid-latitude position of the site, climatic conditions resembled today's
507 Mediterranean climate throughout the "Zone Salifère Moyenne", with distinct wet (winter) and dry
508 (summer) seasons (Schuler, 1988). Furthermore, these mudstone-anhydrite couplets are similar to
509 varves from the late Pleistocene Lisan Formation (Dead Sea, Israel) (Ben Dor et al., 2019), which are
510 composed of endogenic aragonite and gypsum laminae precipitating during dry summers, and detrital-
511 rich laminae deposited during winter runoff. We therefore consider the thin mudstone-anhydrite couplets
512 of the DP-XXVIII well as endogenic-clastic varves, comparable to those of the Dead Sea, even though
513 processes might differ following water balance conditions.



514

515 **Figure 9:** Interpretative deposition model for the formation of three types of varves identified for the
 516 southern Upper Rhine Graben through the late Priabonian and Rupelian. The main climate variation
 517 that causes the seasonality of depositional processes are the changes in precipitation due to dry
 518 summers and humid winters.

519 The anhydrite pseudomorphs overlying bottom-nucleated gypsum and thin crystal (anhydrite
 520 cumulates) couplets of the 1029.3 m sample could also be varves, but these were deposited under drier
 521 conditions than the mudstone-anhydrite examples (Figure 4). The first ones are similar to seasonal
 522 temperature-driven couplets described in the Dead Sea, which are composed of alternations of coarse
 523 and fine halite or gypsum crystals (Sirota et al., 2017; Ben Dor et al., 2019).

524 5.1.2.2. Proximal records (Altkirch and Kleinkems quarries; “Zone Fossilifère”)

525 The samples from the Altkirch (southern river fan delta) and Kleinkems (fan-delta related to the eastern
 526 border fault; Düringer, 1988) quarries display couplets of dark- and light-colored laminae. The light-
 527 colored laminae contain large amounts of detrital silt-sized grains. We propose that they were delivered
 528 by fluvial runoff during the wet season. Grains comprise a diverse mineral assemblage, with calcite and
 529 quartz derived from the erosion of the surrounding uplifted Mesozoic (and Paleozoic) rift shoulders.
 530 While quartz grains are clearly detrital, calcite crystals could either be autochthonous or allochthonous
 531 (e.g., reworked from Jurassic limestones). In the case of the Altkirch Quarry, the presence of organic
 532 matter, mostly alongside detrital grains, suggests that it is of detrital origin. Furthermore, terrestrial
 533 macrofossils such as plant debris account for a fluvial sediment source in these deposits (Figure 6B;
 534 Gaudant & Burkhardt, 1984; Düringer, 1988). The light-colored laminae show fining-up sequences,
 535 which suggests that they record a flood (pulse event) during the wet season, rather than a continuous
 536 accumulation of sediment through multiple months. The varying thickness of these laminae could reflect
 537 year-to-year climatic variability, with the thicker laminae possibly representing winters with more intense
 538 precipitation. However, this could also be explained solely by internal fluvial processes, such as channel
 539 migration or sediment availability. The dark-colored laminae are homogenous and made of thin micrite
 540 (likely aragonite) crystals. The absence of lithogenic elements (Si, Fe, K) in the dark-colored laminae
 541 indicates the absence of detrital material, which suggests that the micrite crystals are endogenic
 542 (formed in the water column) rather than detrital. These interpretations are supported by the elemental

543 profiles that clearly distinguish between endogenic carbonated laminae (enriched in Ca with no
544 lithogenic elements) and detrital laminae (enriched in lithogenic elements; Figure 5). Furthermore, these
545 couplets are very similar to the Holocene clastic-calcitic varves of Lake Chatyr Kol, for which the
546 seasonal deposition pattern is supported by radiometric dating, even though they contain less sub-
547 layers (Kalanke et al., 2020). These varves exhibit a detrital layer with a sharp basal boundary (runoff),
548 with chrysophytes and/or diatoms occurring after or within it, overlain by a layer of endogenic
549 (evaporation) and fine-grain detrital calcite, which is topped by an amorphous organic matter sub-layer.
550 Therefore, by comparison with the varves of Lake Chatyr Kol, and according to petrographical and
551 geochemical evidence presented in this study, we interpret the clastic-endogenic couplets of the Altkirch
552 Quarry as varves.

553 In the case of the Kleinkems Quarry, the presence of lithogenic elements in the dark-colored laminae
554 suggests a persistent input of detrital material even during the dry season. This observation leads us to
555 the interpretation of both the dark- and light-colored laminae couplets of this quarry as solely clastic
556 varves that show seasonal changes in grain-size. However, it is not impossible that the dark-colored
557 laminae are endogenic (similarly to the clastic-calcitic varves of Lake Chatyr Kol; Kalanke et al., 2020),
558 and that the proximity of the depositional area with the border fault accounts for occasional detrital input.

559 5.1.2.3. Sediment Accumulation Rates

560 Considering the ~2 mm varve thickness of the “Sel III” unit (Figure 4), the average SAR is estimated at
561 ~2 m/kyr. This SAR would imply that precession cycles would be ~40 m thick, which is much more than
562 the observed ~12.6 m thick mudstone-evaporite alternations of the “Sel III” unit. It would also imply a
563 SAR higher than any observed rift valley (Schwab, 1976). This estimation however does not account
564 for the potential SAR variations across lithologies, and especially when considering the mudstone
565 intervals, as not all mudstone samples are finely laminated (Figure 3F; see supplementary files). Precise
566 estimates cannot be given here due to the fragmentary nature of the retrieved core samples. Further
567 studies are required to provide more details, such as continuous microfacies descriptions (which would
568 require the collection of new core). However, in the case of the lowermost “Zone Salifère Supérieure”,
569 SARs from fine laminations interpreted as varves (Kühn & Roth, 1979) have been used to interpret that
570 the decimeter-thick mudstone-evaporite alternations are as induced by precession in the MAX borehole
571 (Blanc-Valleron et al., 1989; Blanc-Valleron, 1990). We performed the spectral analysis of a part of the
572 “Zone Salifère Supérieure” to provide an independent argument for the interpretation of the meter-thick
573 to decimeter-thick mudstone-evaporite alternations as being astronomically-forced (Figure 8).

574 5.2. Cycle interpretation

575 The ratios between the ~82.3 m, ~22.4 m, ~9 m, and ~4.5 sedimentary cycles (DP-212 well, “Sel V”) in
576 the depth domain (18.3 : 5 : 2 : 1) (Figure 8) are particularly close to those of the orbital cycles (long
577 eccentricity, short eccentricity, obliquity, and precession) in the time domain (20 : 5 : 2 : 1). The ~82.3
578 m cycle is therefore interpreted as corresponding to the long eccentricity, the ~22.4 m cycle to short
579 eccentricity, the ~9 m cycle to obliquity, and the ~4.5 m cycle to precession. Furthermore, the ~4.5 m
580 sedimentary cycle has three main peaks that can be correlated to the three main periods of precession.
581 The fact that the ~4.5 m cycle is in phase with the majority of observed mudstone-evaporite alternations
582 suggests that they were primarily induced by precession through the “Sel V” unit (Figure 8). By
583 comparison, this interpretation confirms the previous investigation of Blanc-Valleron et al. (1989) that
584 suggests that the mudstone-evaporite cycles of the “Sel III” were astronomically-forced.

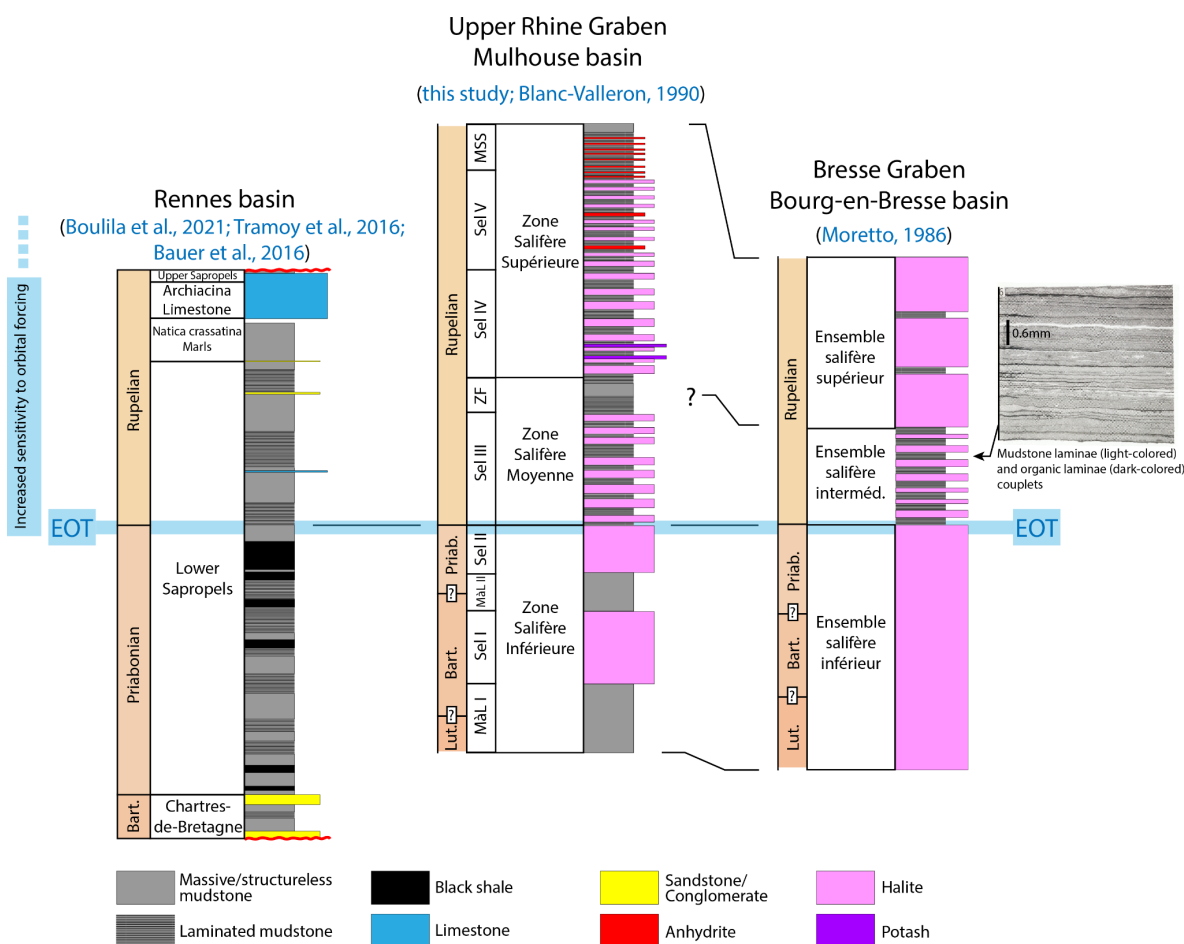
585 5.3. Facies change across the EOT: a marker of regional climatic change with implications for 586 global climate dynamics

587 The facies transition from massive mudstones to laminated sediments and varves along the onset of
588 the meter-thick to decimeter-thick mudstone-evaporite alternations is well-documented in the original
589 description of the DP-XXVIII well (MDPA, 1960). Until now, it was neither discussed, nor placed in the
590 perspective of the EOT (Figure 2, Figure 3). The two main drivers of change in sedimentary facies are
591 climate and tectonics (Carroll & Bohacs, 1999). The climatic evolution of the URG during the Eocene
592 and Oligocene is relatively well-known and reveals a marked increase in the seasonal climatic contrast
593 at the bottom of the “Sel III” unit (Schuler, 1988). Climatic conditions shifted from wet subtropical during
594 the “Zone Salifère Inférieure”, with a short or absent dry season, to the drier subtropical/mediterranean-

595 type conditions of the “Zone Salifère Moyenne”, with a pronounced dry season lasting around half the
596 year. This shift is penecontemporaneous with the facies transition, and we therefore argue that this
597 change in sedimentary facies reflects the onset of a pronounced seasonal climatic contrast. In addition,
598 the onset of laminated sediments and varves is also synchronous with the onset of repetitive decimeter-
599 thick marl-evaporite alternations. The study of Blanc-Valleron et al. (1989), and the spectral analysis of
600 the DP-212 well presented in this paper, suggest that these alternations are forced by precession in the
601 “Zone Salifère Supérieure” (Figure 2, Figure 8), and in the “Sel III” as well by comparison.

602 In paleoenvironmental terms of the classification of lake-basin types (Carroll & Bohacs, 1999; Bohacs
603 et al., 2000), the deposits of the “Zone Salifère Inférieure”, “Zone Salifère Moyenne”, and “Zone Salifère
604 Supérieure” are characteristic of an underfilled lake. The relative stability of the climate across the
605 deposition of the “Zone Salifère Inférieure” (Schuler, 1988) suggests that these lithological changes
606 were potentially not driven by climatic changes. Starting from the bottom of the “Sel III”, the decimeter-
607 thick mudstone-evaporite cycles were most likely induced by lake-level variations related to orbital
608 cycles. While we emphasize that the varves resulted from seasonal precipitation changes, with the
609 clastic laminae being deposited during humid winters and chemical laminae deposited during dry
610 summers (potentially associated to seasonal lake-level fluctuations), it is also possible that seasonal
611 temperature changes influenced the saturation of brines. By comparison, facies changes associated
612 with an increase in seasonal climatic contrast have been documented further west in the Rennes Basin
613 across the EOT (Tramoy et al., 2016; Bauer et al., 2016; Boulila et al., 2021). In the Rennes Basin, a
614 sharp contact between massive, clotted greenish clays, and brownish, organic laminated clays is
615 described above the Eocene-Oligocene boundary (Oi-1 event) (Boulila et al., 2021). However, the
616 microfacies of the laminated clays were not analyzed in detail and their depositional processes and
617 potential cyclicity (i.e., as varved deposits) were not assessed. Furthermore, laminated mudstones are
618 also described earlier in the sequence and are attributed to hypoxic lacustrine conditions. Detailed
619 microfacies investigations would be required to assess whether these laminated sediments show
620 significant facies changes before and after the EOT. The detailed cyclostratigraphy of the Rennes Basin
621 indicates strengthening of the eccentricity and the precession band at the EOT (Boulila et al., 2021).
622 There are therefore strong similarities between the Mulhouse Basin and the Rennes Basin, as both
623 basins display pronounced facies changes with the presence of laminated sediments and
624 astronomically-forced sedimentary alternations. Furthermore, the Bourg-en-Bresse Basin (Bresse
625 Graben), similar to the Mulhouse Basin, exhibits the onset of decimeter-thick mudstone-evaporite
626 alternations in which mudstones are laminated and display light-colored (carbonated) and dark-colored
627 (organic) sub-millimeter-thick couplets that resemble varves (Moretto, 1986) (Figure 10). The bottom of
628 the “Ensemble Salifère Intermédiaire” of the Bourg-en-Bresse Basin has been correlated to the bottom
629 of the “Sel III” of the Mulhouse Basin (Moretto, 1986; Blanc-Valleron, 1990), and both basins display an
630 increase in seasonal climatic contrast at that time (Schuler, 1988). The combined observations of these
631 three records (which are several hundreds of kilometers apart) provide evidence for an increase in
632 seasonal climatic contrast and in sensitivity of the climate to orbital variations over the continental west
633 European mid-latitudes during the EOT. This hypothesis is consistent with recent studies that suggest
634 an increase in sensitivity of the climate to orbital variations across the EOT (Westerhold et al., 2020;
635 Tardif et al., 2021).

636 This prominent change in sedimentary regime occurs over a short stratigraphic interval and marks a
637 change-point in the evolution of the behavior of the lacustrine systems that occupied the three basins.
638 All these characteristics match well with the definition of a xenoconformity, which describes a
639 stratigraphic surface (or gradational interval) that records an abrupt change in sedimentary facies
640 across regional to global scales (Carroll, 2017). The intra-basinal to inter-basinal recognition of such a
641 singular stratigraphic surface or interval is therefore interpreted as diagnostic of major global climate
642 changes, such as that of the Oi-1 event (and EOT) observed in western Eurasia mid-latitude lacustrine
643 records (Boulila et al., 2016; Ao et al., 2020). We thus propose that the increase in seasonal climatic
644 contrast and sensitivity of climate to orbital variations observed in the Mulhouse and Bourg-en-Bresse
645 basins are, similarly, synchronous with the EOT.



646

647 **Figure 10:** Comparison and correlations between the sedimentary records of the Rennes (Bauer et al.,
648 2016; Tramoy et al., 2016; Bouilila et al., 2021), Mulhouse (Blanc-Valleron, 1990; this study), and Bourg-
649 en-Bresse (Moretto, 1986) basins.

650 Compared to investigations performed at other localities, our findings better assess regional and global
651 coherency (and therefore potential driving mechanisms) of the observed changes. High resolution
652 marine $\delta^{13}\text{C}$ and $\delta^{18}\text{O}$ benthic records suggest increased sensitivity of the climate to orbital variations
653 across the EOT, which are linked to the formation of the Antarctic ice sheet and resulting increased
654 oceanic circulation dynamics at seasonal and orbital scales (see Westerhold et al., 2020 and references
655 therein). This provides a simple explanation for the increased seasonal climatic contrast observed in
656 western Europe and is substantiated by further studies. The study of North Atlantic sediment cores
657 revealed the change from diverse mixed broad-leaved to cooler conifer-dominated pollen, indicative of
658 an increase in seasonal climatic contrast across the EOT (Eldrett et al., 2009). Geochemical analyses
659 performed on shells of freshwater gastropods in the Hampshire Basin (United Kingdom) indicate a
660 decrease in growing-season surface temperatures of 4°C across the EOT, indicating that the change
661 in seasonal climatic contrast was likely also expressed by colder winters (Hren et al., 2013). Other
662 studies account for a shift from warm paratropical/temperate to temperate/boreal vegetation in western
663 and central Europe, which is also indicative of an increase in seasonal climatic contrast across the EOT
664 (Mosbrugger et al., 2005; Kvaček et al., 2014; Utescher et al., 2015; Kunzmann et al., 2016). Continental
665 temperature curves derived from central Europe flora have been correlated to global marine oxygen
666 isotopes, suggesting a tight link between continental climate with oceanic changes and Antarctic ice-
667 sheet (Mosbrugger et al., 2005), as well as the interpretation that pCO_2 drawdown and associated
668 temperature drop that may have simply led to dryer and cooler winters, thus enhancing seasonal
669 climatic contrasts (Eldrett et al., 2009). Furthermore, these observations are similar to a distant record
670 in northeastern Tibet, where a transition from sedimentary cycles dominated by eccentricity to
671 sedimentary cycles paced by a combination of eccentricity, obliquity, and precession is observed across
672 the Oi-1 event (Ao et al., 2020). This suggests increased seasonality extended at least over the
673 Eurasian continent across the EOT. However, this trend does not appear to extend globally, as indicated
674 by recent proxy-data reviews across the EOT (Hutchinson et al., 2019) and data-model comparisons

675 (Tardif et al., 2021; Toumoulin et al., 2022), most notably in North America showing only limited
676 variability increases. This implies the EOT affected Eurasia climate patterns differently and led to the
677 suggested increase in modulations of the westerlies (Toumoulin et al., 2022). Most importantly,
678 teleconnections in circulation changes in the North Atlantic following the formation of the Antarctic ice-
679 sheet has been proposed to relate to the onset and/or strengthening of the AMOC (Goldner et al., 2014).
680 Such a mechanism would affect the seasonal climatic contrast and the sensitivity of local climate to
681 orbital forcing in Eurasian mid-latitude records (Goldner et al., 2014). It should be noted, however, that
682 more recent numerical simulations considering the pCO₂ reduction, the Antarctic ice-sheet
683 development, as well as gateway opening around Antarctica associated with sea-level drop, fail to
684 reproduce strengthening of AMOC-like oceanic dynamics (see Toumoulin et al., 2020 and references
685 therein). Recent studies have also linked the EOT to gateway opening and closing between the Atlantic
686 and the proto-Arctic (Coxall et al., 2018; Straume et al., 2022). These changes may have affected
687 atmospheric and oceanic circulation globally and certainly induced changes in western Europe during
688 the EOT.

689 Further investigations are required to determine more precisely the links and contributions between
690 global drivers such as pCO₂ drawdown, sea-level drop, and tectonically-forced changes in oceanic
691 circulation (Kennett, 1977; DeConto & Pollard, 2003; Pearson et al., 2009; Abelson & Erez, 2017;
692 Toumoulin et al., 2020; Straume et al., 2022) of European climates across the EOT. This requires the
693 determination of the exact timing of the observed changes in seasonality and astronomically-forced
694 cyclicity through the various phases of the EOT (e.g., Boulila et al., 2021), in combination with numerical
695 model simulations focusing on these particular entities.

696 6. Conclusion

697 This paper provides insights into the enhancement of seasonal climatic contrast and sensitivity of the
698 local climate to orbital variations across the Eocene-Oligocene Transition in the Upper Rhine Graben.
699 Our new results are based on analyses of sedimentary rock cores and documents from the DP-XXVIII
700 and DP-212 wells, as well as rock samples from the Altkirch and Kleinkems quarries (proximal records;
701 “Zone Fossilifère”). Our investigation provides a new perspective on climate change during the Eocene-
702 Oligocene Transition, the impact upon the lacustrine record of the Upper Rhine Graben, and how this
703 related to global climate dynamics.

- 704 1. The presence of varves in the “Sel III” and “Zone Fossilifère” units of the DP-XXVIII well, and
705 in the “Zone Fossilifère” unit of the Altkirch and Kleinkems quarries is proposed based on
706 microfacies analysis, together with a model combining fabric formation and depositional
707 hydrology. We compared the lower Oligocene varves of the Mulhouse Basin to those from
708 the Dead Sea (Ben Dor et al., 2019), and the varves of the Altkirch and Kleinkems quarries
709 (“Zone Fossilifère”) to those from the Chatyr Kol Lake (Kalanke et al., 2020).
- 710 2. In the DP-XXVIII well, a strong facies transition from massive mudstones to laminated and
711 varved mudstones is documented from the base of the “Sel III” unit. This change in
712 sedimentary pattern coincides with the onset of decimeter-thick mudstone-evaporite cycles,
713 which we demonstrate are induced by orbital variations. Palynological studies have shown a
714 penecontemporaneous change in climatic conditions towards a mediterranean climate with
715 enhanced seasonal climatic contrast (Schuler, 1988). We thus propose that the appearance
716 of the laminated and varved mudstones records a stronger contrast in the sedimentation
717 processes that resulted from the climate change towards a stronger seasonal climatic
718 contrast. We also suggest that the onset of the decameter-thick mudstone-evaporite cycles
719 is related to an increase of the sensitivity of the climate to orbital variations across the EOT.
- 720 3. We outlined similarities between our observations in the Upper Rhine Graben and changes
721 in sedimentary facies documented in the Rennes Basin during the Eocene-Oligocene
722 Transition (Boulila et al., 2021), and in the Bourg-en-Bresse Basin (Moretto, 1986). As such,
723 we suggest that this spatially-transgressive facies transition could be the marker of the
724 Eocene-Oligocene Transition in European mid-latitude lacustrine records. By comparison
725 with similar observations performed in northeastern Tibet, this change could be a marker of
726 the Oi-1 event (Ao et al., 2020). The characterization of such changes in sedimentary facies
727 could help understand climate change during the Eocene-Oligocene Transition and aid the
728 establishment of chronological frameworks. In addition, we suggest that the abruptness of
729 this transition in the Mulhouse, Bourg-en-Bresse, and Rennes basins could reflect a

730 changepoint that had a major impact on regional climate, possibly through a pCO₂ drop
731 and/or oceanic circulation changes, such as the onset of a proto-AMOC in relation with the
732 formation of the Antarctic icesheet. We also show that these observations are coherent with
733 other coeval paleoclimatic records in Europe.

734 **Acknowledgements**

735 We are grateful to the Musée d'Histoire Naturelle et d'Ethnographie de Colmar (Martial BOUTANTIN,
736 Claitre PRÊTRE, Manuelle VIGNES) for providing access to the core samples from the DP-XXVIII well,
737 and to the Kalivie Museum (Chantal VIS, Loïc DEMESY) for providing access to the original written
738 descriptions by MDPA of the DP-XXVIII well. We thank Magalie LINDENMAYER from the Holcim
739 Quarry in Altkirch for allowing us to retrieve samples from the quarry. We thank Kirsten GRIMM and
740 Matthias GRIMM for insightful discussions on the biostratigraphy of the Upper Rhine Graben. The PhD
741 of ES is funded by MESRI and Région Grand-Est. Field work and analysis were funded by a research
742 grant from CNRS/INSU (TelluS/SysTer program) attributed to MS. Additional support was provided by
743 the "Geological Systems" research team at ITES. We are grateful to Ola KWIECIEN and Nicolas
744 WALDMANN for reviewing the manuscript and providing insightful comments.

745 **Conflict of Interest**

746 The authors declare no conflict of interest.

747 **Data Availability**

748 All the data presented in this publication can be downloaded from the website of *Sedimentologia*.

749 **Authors contributions**

750 ES wrote the paper, performed sedimentary facies analysis (with LGC, FG, HV and MS). All authors
751 contributed to interpretation and discussion of the results. ES and MS worked on the illustrations and
752 collected field samples. ES and LGC worked on the logging and description of the DP-XXVIII well. MU
753 performed the μ -XRF analyses and helped the interpretation. ES and CB worked on the μ -XRF results
754 and on the interpretation of varves and laminated sediments. MS and HV designed the overall research
755 project dedicated to the EOT in the URG, and group discussions allowed to sharply define the topic of
756 this paper. GDN provided insights and discussions in regard to the EOT. MM provided insights and
757 discussions in regard to cyclostratigraphy and paleoclimates. LGC provided insights and discussions
758 on evaporites, cores, and on the URG. FG provided insights and discussions on the URG and cores.
759 CB, LGC, HV and MS provided expertise on laminated sediments and varves.

760 **References**

- 761 Abelson, M., & Erez, J. (2017). The onset of modernlike Atlantic meridional overturning circulation at
762 the Eocene-Oligocene transition: Evidence, causes, and possible implications for global cooling.
763 *Geochemistry, Geophysics, Geosystems*, 18(6), 2177-2199. <https://doi.org/10.1002/2017GC006826>
- 764 Aichholzer, C. (2019). Le log complet de la stratigraphie de la zone rhénane ainsi que les modalités
765 stratigraphiques, sédimentaires et structurales de la transition socle-couverture: application à la
766 géothermie profonde (Doctoral dissertation, Université de Strasbourg).
- 767 Ao, H., Dupont-Nivet, G., Rohling, E. J., Zhang, P., Ladant, J. B., Roberts, A. P., Licht, A., Liu, Q., Liu,
768 Z., Dekkers, M. J., Coxall, H. K., Jin, Z., Huang, C., Xiao, G., Poulsen, C. J., Barbolini, N., Meijer, N.,
769 Sun, Q., Qiang, X., Yao, J., & An, Z. (2020). Orbital climate variability on the northeastern Tibetan
770 Plateau across the Eocene–Oligocene transition. *Nature communications*, 11(1), 5249.
771 <https://doi.org/10.1038/s41467-020-18824-8>

- 772 Bauer, H., Bessin, P., Saint-Marc, P., Châteauneuf, J. J., Bourdillon, C., Wyns, R., & Guillocheau, F.
773 (2016). The Cenozoic history of the Armorican Massif: New insights from the deep CDB1 borehole
774 (Rennes Basin, France). *Comptes Rendus Geoscience*, 348(5), 387-397.
775 <https://doi.org/10.1016/j.crte.2016.02.002>
- 776 Ben Dor, Y. B., Neugebauer, I., Enzel, Y., Schwab, M. J., Tjallingii, R., Erel, Y., & Brauer, A. (2019).
777 Varves of the Dead Sea sedimentary record. *Quaternary Science Reviews*, 215, 173-184.
778 <https://doi.org/10.1016/j.quascirev.2019.04.011>
- 779 Berger, J. P., Reichenbacher, B., Becker, D., Grimm, M., Grimm, K., Picot, L., Storni, A., Pirkenseer,
780 C., & Schaefer, A. (2005). Eocene-Pliocene time scale and stratigraphy of the Upper Rhine Graben
781 (URG) and the Swiss Molasse Basin (SMB). *International Journal of Earth Sciences*, 94, 711-731.
782 <https://doi.org/10.1007/s00531-005-0479-y>
- 783 Blanc-Valleron, M. M. (1990). Les formations paléogènes évaporitiques du bassin potassique de
784 Mulhouse et des bassins plus septentrionaux d'Alsace. Documents BRGM, Vol. 204, 350 p.
- 785 Blanc-Valleron, M. M., Foucault, A., & Gannat, E. (1989). Le contrôle climatique, orbital, et solaire de
786 la sédimentation évaporitique : exemple de la base du Salifère supérieur (Oligocène inférieur) du bassin
787 de Mulhouse (Sud du fossé rhénan, France). *Comptes rendus de l'Académie des sciences. Série 2,*
788 *Mécanique, Physique, Chimie, Sciences de l'univers, Sciences de la Terre*, 308(4), 435-441.
- 789 Boës, X., Rydberg, J., Martinez-Cortizas, A., Bindler, R., & Renberg, I. (2011). Evaluation of
790 conservative lithogenic elements (Ti, Zr, Al, and Rb) to study anthropogenic element enrichments in
791 lake sediments. *Journal of Paleolimnology*, 46, 75-87. <https://doi.org/10.1007/s10933-011-9515-z>
- 792 Bohacs, K. M., Carroll, A. R., Neal, J. E., & Mankiewicz, P. J. (2000). Lake-Basin Type, Source Potential,
793 and Hydrocarbon Character: an Integrated Sequence-Stratigraphic-Geochemical Framework, in E. H.
794 Gierlowski-Kordesch and K. R. Kelts, eds., *Lake basins through space and time: AAPG Studies in*
795 *Geology*, 46, 3–34. <https://doi.org/10.1306/St46706C1>
- 796 Bohaty, S. M., Zachos, J. C., & Delaney, M. L. (2012). Foraminiferal Mg/Ca evidence for Southern
797 Ocean cooling across the Eocene–Oligocene transition. *Earth and Planetary Science Letters*, 317, 251-
798 261. <https://doi.org/10.1016/j.epsl.2011.11.037>
- 799 Boulila, S., Dupont-Nivet, G., Galbrun, B., Bauer, H., & Châteauneuf, J. J. (2021). Age and driving
800 mechanisms of the Eocene–Oligocene transition from astronomical tuning of a lacustrine record
801 (Rennes Basin, France). *Climate of the Past*, 17(6), 2343-2360. [https://doi.org/10.5194/cp-17-2343-
802 2021](https://doi.org/10.5194/cp-17-2343-2021)
- 803 Brauer, A., Dulski, P., Mangili, C., Mingram, J., & Liu, J. (2009). The potential of varves in high-resolution
804 paleolimnological studies. *PAGES news*, 17(3), 96-98. <https://doi.org/10.22498/pages.17.3.96>
- 805 Carroll, A.R., 2017, Xenconformities and the stratigraphic record of paleoenvironmental change:
806 *Geology*, v. 45, p. 639–642. <https://doi.org/10.1130/G38952.1>
- 807 Carroll, A. R., & Bohacs, K. M. (1999). Stratigraphic classification of ancient lakes: Balancing tectonic
808 and climatic controls. *Geology*, 27(2), 99-102. [https://doi.org/10.1130/0091-
809 7613\(1999\)027<0099:SCOALB>2.3.CO;2](https://doi.org/10.1130/0091-7613(1999)027<0099:SCOALB>2.3.CO;2)
- 810 Châteauneuf, J. J., & Ménéillet, F. (2014). A Bartonian microflora record from the Upper Rhine Graben:
811 the Mietesheim formation (Alsace, France). *Géologie de la France*, (1), 3-20.
- 812 Courtot, C., Gannat, E., & Wendling, E. (1972). Le bassin potassique de Mulhouse et ses environs.
813 *Étude du Tertiaire. Sciences Géologiques, bulletins et mémoires*, 25(2), 69-91.
- 814 Coxall, H. K., Huck, C. E., Huber, M., Lear, C. H., Legarda-Lisarrri, A., O'regan, M., Sliwiska K. K., van
815 de Flierd, T., de Boer, A. M., Zachos, J. C., & Backman, J. (2018). Export of nutrient rich Northern
816 Component Water preceded early Oligocene Antarctic glaciation. *Nature Geoscience*, 11(3), 190-196.
817 <https://doi.org/10.1038/s41561-018-0069-9>

- 818 Coxall, H. K., Wilson, P. A., Pälike, H., Lear, C. H., & Backman, J. (2005). Rapid stepwise onset of
819 Antarctic glaciation and deeper calcite compensation in the Pacific Ocean. *Nature*, 433(7021), 53-57.
820 <https://doi.org/10.1038/nature03135>
- 821 Davies, S. J., Lamb, H. F., & Roberts, S. J. (2015). Micro-XRF Studies of Sediment Cores: Applications
822 of a non-destructive tool for the environmental sciences. *Developments in Paleoenvironmental*
823 *Research*, 17, 189-226. https://doi.org/10.1007/978-94-017-9849-5_7
- 824 DeConto, R. M., & Pollard, D. (2003). Rapid Cenozoic glaciation of Antarctica induced by declining
825 atmospheric CO₂. *Nature*, 421(6920), 245-249. <https://doi.org/10.1038/nature01290>
- 826 Dèzes, P., Schmid, S. M., & Ziegler, P. A. (2004). Evolution of the European Cenozoic Rift System:
827 interaction of the Alpine and Pyrenean orogens with their foreland lithosphere. *Tectonophysics*, 389(1-
828 2), 1-33. <https://doi.org/10.1016/j.tecto.2004.06.011>
- 829 Dräger, N., Theuerkauf, M., Szeroczyńska, K., Wulf, S., Tjallingii, R., Plessen, B., Kienel, U., & Brauer,
830 A. (2017). Varve microfacies and varve preservation record of climate change and human impact for
831 the last 6000 years at Lake Tiefer See (NE Germany). *The Holocene*, 27(3), 450-464.
832 <https://doi.org/10.1177/0959683616660173>
- 833 Dupont-Nivet, G., Krijgsman, W., Langereis, C. G., Abels, H. A., Dai, S., & Fang, X. (2007). Tibetan
834 plateau aridification linked to global cooling at the Eocene–Oligocene transition. *Nature*, 445(7128),
835 635-638. <https://doi.org/10.1038/nature05516>
- 836 Düringer, P. (1988). Les conglomérats des bordures du rift cénozoïque rhénan : dynamique
837 sédimentaire et contrôle climatique. Thèse d'État, Université de Strasbourg, 287p.
- 838 Edel, J. B., Schulmann, K., & Rotstein, Y. (2007). The Variscan tectonic inheritance of the Upper Rhine
839 Graben: evidence of reactivations in the Lias, Late Eocene–Oligocene up to the recent. *International*
840 *Journal of Earth Sciences*, 96(2), 305-325. <https://doi.org/10.1007/s00531-006-0092-8>
- 841 Eldrett, J. S., Greenwood, D. R., Harding, I. C., & Huber, M. (2009). Increased seasonality through the
842 Eocene to Oligocene transition in northern high latitudes. *Nature*, 459(7249), 969-973.
843 <https://doi.org/10.1038/nature08069>
- 844 Förster B. (1911). Ergebnisse der Untersuchung von Bohrproben aus den seit 1904 im Gange
845 befindlichen, zur Aufsuchung von Steinsalz und Kalisaltzen ausgeführten Tiefbohrungen im Tertiär des
846 Oberelsass. *Mitt. Geol. Landesanst. Els.-Lothr.*, 7(4), 349-524.
- 847 Gaudant, J., & Burkhardt, T. (1984). Sur la découverte de poissons fossiles dans les marnes grises
848 rayées de la zone fossilifère (Oligocène basal) d'Altkirch (Haut-Rhin). *Sciences Géologiques, bulletins*
849 *et mémoires*, 37(2), 153-171.
- 850 Goldner, A., Herold, N., & Huber, M. (2014). Antarctic glaciation caused ocean circulation changes at
851 the Eocene–Oligocene transition. *Nature*, 511(7511), 574-577. <https://doi.org/10.1038/nature13597>
- 852 Grimm, M. C., Wielandt-Schuster, U., Hottenrott, M., Radtke, G., Berger, J. P., Ellwanger, D., Harms,
853 F. J., Hoselmann, C. P., & Weidenfeller, M. (2011). Oberrheingraben (Tertiär des Oberrheingrabens).
854 *Schriftenreihe der Deutschen Gesellschaft für Geowissenschaften*, 57-132.
855 <https://doi.org/10.1127/sdgg/75/2011/57>
- 856 Hooker, J. J., Collinson, M. E., & Sille, N. P. (2004). Eocene–Oligocene mammalian faunal turnover in
857 the Hampshire Basin, UK: calibration to the global time scale and the major cooling event. *Journal of*
858 *the Geological Society*, 161(2), 161-172. <https://doi.org/10.1144/0016-764903-091>
- 859 Hren, M. T., Sheldon, N. D., Grimes, S. T., Collinson, M. E., Hooker, J. J., Bugler, M., & Lohmann, K.
860 C. (2013). Terrestrial cooling in Northern Europe during the Eocene–Oligocene transition. *Proceedings*
861 *of the National Academy of Sciences*, 110(19), 7562-7567. <https://doi.org/10.1073/pnas.1210930110>

- 862 Hutchinson, D. K., Coxall, H. K., Lunt, D. J., Steinthorsdottir, M., De Boer, A. M., Baatsen, M., von der
863 Heydy, A., Huber, M., Kennedy-Asser, A. T., Kunzmann, L., Ladant, J. B., Lear, C. H., Moraweck, K.,
864 Pearson, P. N., Piga, E., Pound, M. J., Salzmann, U., Scher, H. D., Sijp, W. P., Śliwińska, K.K., Wilson,
865 P. A., & Zhang, Z. (2021). The Eocene–Oligocene transition: a review of marine and terrestrial proxy
866 data, models and model–data comparisons. *Climate of the Past*, 17(1), 269-315.
867 <https://doi.org/10.5194/cp-17-269-2021>
- 868 Hutchinson, D. K., Coxall, H. K., O'Regan, M., Nilsson, J., Caballero, R., & de Boer, A. M. (2019). Arctic
869 closure as a trigger for Atlantic overturning at the Eocene-Oligocene Transition. *Nature*
870 *Communications*, 10(1), 3797. <https://doi.org/10.1038/s41467-019-11828-z>
- 871 Ivany, L. C., Patterson, W. P., & Lohmann, K. C. (2000). Cooler winters as a possible cause of mass
872 extinctions at the Eocene/Oligocene boundary. *Nature*, 407(6806), 887-890.
873 <https://doi.org/10.1038/35038044>
- 874 Kalanke, J., Mingram, J., Lauterbach, S., Usubaliev, R., Tjallingii, R., & Brauer, A. (2020). Seasonal
875 deposition processes and chronology of a varved Holocene lake sediment record from Chatyr Kol lake
876 (Kyrgyz Republic). *Geochronology*, 2(1), 133-154. <https://doi.org/10.5194/gchron-2-133-2020>
- 877 Katz, M. E., Miller, K. G., Wright, J. D., Wade, B. S., Browning, J. V., Cramer, B. S., & Rosenthal, Y.
878 (2008). Stepwise transition from the Eocene greenhouse to the Oligocene icehouse. *Nature*
879 *geoscience*, 1(5), 329-334. <https://doi.org/10.1038/ngeo179>
- 880 Kennedy, A. T., Farnsworth, A., Lunt, D. J., Lear, C. H., & Markwick, P. J. (2015). Atmospheric and
881 oceanic impacts of Antarctic glaciation across the Eocene–Oligocene transition. *Philosophical*
882 *Transactions of the Royal Society A: Mathematical, Physical and Engineering Sciences*, 373(2054),
883 20140419. <https://doi.org/10.1098/rsta.2014.0419>
- 884 Kennett, J. P. (1977). Cenozoic evolution of Antarctic glaciation, the circum-Antarctic Ocean, and their
885 impact on global paleoceanography. *Journal of geophysical research*, 82(27), 3843-3860.
886 <https://doi.org/10.1029/JC082i027p03843>
- 887 Kohn, M. J., Strömberg, C. A., Madden, R. H., Dunn, R. E., Evans, S., Palacios, A., & Carlini, A. A.
888 (2015). Quasi-static Eocene–Oligocene climate in Patagonia promotes slow faunal evolution and mid-
889 Cenozoic global cooling. *Palaeogeography, Palaeoclimatology, Palaeoecology*, 435, 24-37.
890 <https://doi.org/10.1016/j.palaeo.2015.05.028>
- 891 Kühn, R., & Roth, H. (1979). Beiträge zur Kenntnis der Salzlagerstätte am Oberrhein. *Z. Geol. Wiss.*,
892 7, 953-966.
- 893 Kunzmann, L., Kvaček, Z., Teodoridis, V., Müller, C., & Moraweck, K. (2016). Vegetation dynamics of
894 riparian forest in central Europe during the late Eocene. *Palaeontographica Abteilung B*, 69-89.
895 <https://doi.org/10.1127/palb/295/2016/69>
- 896 Kvaček, Z., Teodoridis, V., Mach, K., Prikryl, T., & Dvořák, Z. (2014). Tracing the Eocene-Oligocene
897 transition: a case study from North Bohemia. *Bulletin of Geosciences*, 89(1).
898 <https://doi.org/10.3140/bull.geosci.1411>
- 899 Kwiecien, O., Braun, T., Brunello, C. F., Faulkner, P., Hausmann, N., Helle, G., Hoggarth, J. A., Ionita,
900 M., Jazwa, C. S., Kelmelis, S., Marwan, N., Nava-Fernandez, C., Nehme, C., Opel, T., Oster, J. L.,
901 Perşoiu, A., Petrie, C., Prufer, K., Saarni, S. M., Wolf, A., & Breitenbach, S. F. (2022). What we talk
902 about when we talk about seasonality—A transdisciplinary review. *Earth-Science Reviews*, 225, 103843.
903 <https://doi.org/10.1016/j.earscirev.2021.103843>
- 904 Ladant, J. B., Donnadieu, Y., Lefebvre, V., & Dumas, C. (2014). The respective role of atmospheric
905 carbon dioxide and orbital parameters on ice sheet evolution at the Eocene-Oligocene transition.
906 *Paleoceanography*, 29(8), 810-823. <https://doi.org/10.1002/2013PA002593>
- 907 Lear, C. H., Bailey, T. R., Pearson, P. N., Coxall, H. K., & Rosenthal, Y. (2008). Cooling and ice growth
908 across the Eocene-Oligocene transition. *Geology*, 36(3), 251-254. <https://doi.org/10.1130/G24584A.1>

- 909 Li, M., Hinnov, L., & Kump, L. (2019). Acycle: Time-series analysis software for paleoclimate research
910 and education. *Computers & Geosciences*, 127, 12-22. <https://doi.org/10.1016/j.cageo.2019.02.011>
- 911 Liu, Z., Pagani, M., Zinniker, D., DeConto, R., Huber, M., Brinkhuis, H., Shah, S. R., Leckie, R. M., &
912 Pearson, A. (2009). Global cooling during the Eocene-Oligocene climate transition. *Science*, 323(5918),
913 1187-1190. <https://doi.org/10.1126/science.1166368>
- 914 Maïkovsky, V. (1941). Contribution à l'étude paléontologique et stratigraphique du bassin potassique
915 d'Alsace. *Mémoires du Service de la Carte géologique d'Alsace et de Lorraine*, Vol. 6, 192 p.
- 916 Mann, M. E., & Lees, J. M. (1996). Robust estimation of background noise and signal detection in
917 climatic time series. *Climatic change*, 33(3), 409-445. <https://doi.org/10.1007/BF00142586>
- 918 MDPA (1960). Catalogue des puits et sondages du bassin de Mulhouse, Vol. XIV, 3-119. Miller, K. G.,
919 Browning, J. V., Schmelz, W. J., Kopp, R. E., Mountain, G. S., & Wright, J. D. (2020). Cenozoic sea-
920 level and cryospheric evolution from deep-sea geochemical and continental margin records. *Science*
921 *advances*, 6(20), <https://doi.org/10.1126/sciadv.aaz1346>
- 922 Miller, K. G., Browning, J. V., Schmelz, W. J., Kopp, R. E., Mountain, G. S., & Wright, J. D. (2020).
923 Cenozoic sea-level and cryospheric evolution from deep-sea geochemical and continental margin
924 records. *Science Advances*, 6(20), eaaz1346. <https://doi.org/10.1126/sciadv.aaz1346>
- 925 Miller, K. G., Wright, J. D., & Fairbanks, R. G. (1991). Unlocking the ice house: Oligocene-Miocene
926 oxygen isotopes, eustasy, and margin erosion. *Journal of Geophysical Research: Solid Earth*, 96(B4),
927 6829-6848. <https://doi.org/10.1029/90JB02015>
- 928 Mingram, J. (1998). Laminated Eocene maar-lake sediments from Eckfeld (Eifel region, Germany) and
929 their short-term periodicities. *Palaeogeography, Palaeoclimatology, Palaeoecology*, 140(1-4), 289-305.
930 [https://doi.org/10.1016/S0031-0182\(98\)00021-2](https://doi.org/10.1016/S0031-0182(98)00021-2)
- 931 Moretto, R. (1986). Étude sédimentologique et géochimique des dépôts de la série salifère paléogène
932 du bassin de Bourg-en-Bresse (France) (Doctoral dissertation, Université de Lorraine).
- 933 Mosbrugger, V., Utescher, T., & Dilcher, D. L. (2005). Cenozoic continental climatic evolution of Central
934 Europe. *Proceedings of the National Academy of Sciences*, 102(42), 14964-14969.
935 <https://doi.org/10.1073/pnas.0505267102>
- 936 Ojala, A. E., Francus, P., Zolitschka, B., Besonen, M., & Lamoureux, S. F. (2012). Characteristics of
937 sedimentary varve chronologies—a review. *Quaternary Science Reviews*, 43, 45-60.
938 <https://doi.org/10.1016/j.quascirev.2012.04.006>
- 939 Page, M., Licht, A., Dupont-Nivet, G., Meijer, N., Barbolini, N., Hoorn, C., Schauer, A., Huntington, K.,
940 Bajnai, D., Fiebig, J., Mulch, A., & Guo, Z. (2019). Synchronous cooling and decline in monsoonal
941 rainfall in northeastern Tibet during the fall into the Oligocene icehouse. *Geology*, 47(3), 203-206.
942 <https://doi.org/10.1130/G45480.1>
- 943 Pearson, P. N., Foster, G. L., & Wade, B. S. (2009). Atmospheric carbon dioxide through the Eocene–
944 Oligocene climate transition. *Nature*, 461(7267), 1110-1113. <https://doi.org/10.1038/nature08447>
- 945 Pearson, P. N., McMillan, I. K., Wade, B. S., Jones, T. D., Coxall, H. K., Bown, P. R., & Lear, C. H.
946 (2008). Extinction and environmental change across the Eocene-Oligocene boundary in Tanzania.
947 *Geology*, 36(2), 179-182. <https://doi.org/10.1130/G24308A.1>
- 948 Pirkenseer, C., Spezzaferri, S., & Berger, J. P. (2010). Palaeoecology and biostratigraphy of the
949 Paleogene Foraminifera from the southern Upper Rhine Graben and the influence of reworked
950 planktonic Foraminifera. *Palaeontographica, Palaeontographica, Abt. A: Palaeozoology–Stratigraphy*,
951 293, 1-93.
- 952 Priestley, M. B. (1981). *Spectral analysis and time series: probability and mathematical statistics*.
953 Academic Press, London, 1-890.

- 954 Roussé, S. (2006). Architecture et dynamique des séries marines et continentales de l'oligocène moyen
955 et supérieur du sud du fossé rhénan : Evolution des milieux de dépôt en contexte de rift en marge de
956 l'avant-pays alpin (Doctoral dissertation, Université de Strasbourg).
- 957 Sarkar, S., Basak, C., Frank, M., Berndt, C., Huuse, M., Badhani, S., & Bialas, J. (2019). Late Eocene
958 onset of the proto-Antarctic circumpolar current. *Scientific reports*, 9(1), 10125.
959 <https://doi.org/10.1038/s41598-019-46253-1>
- 960 Schuler, M. (1988). Environnements et paléoclimats paléogènes. Palynologie et biostratigraphie de
961 l'Éocène et de l'Oligocène inférieur dans les fossés rhénan, rhodanien et de Hesse. Documents BRGM,
962 Vol. 190, 503 p.
- 963 Schumacher, M. E. (2002). Upper Rhine Graben: role of preexisting structures during rift evolution.
964 *Tectonics*, 21(1), 6-1. <https://doi.org/10.1029/2001TC900022>
- 965 Schwab, F. L. (1976). Modern and ancient sedimentary basins: comparative accumulation rates.
966 *Geology*, 4(12), 723-727. [https://doi.org/10.1130/0091-7613\(1976\)4<723:MAASBC>2.0.CO;2](https://doi.org/10.1130/0091-7613(1976)4<723:MAASBC>2.0.CO;2)
- 967 Simon, E., Gindre-Chanu, L., Nutz, A., Boesch, Q., Dupont-Nivet, G., Vogel, H., Schuster, M. (2021).
968 Regard sur un changement climatique majeur : la transition Éocène-Oligocène dans le Fossé Rhénan.
969 *Géologues*, 210, 26-34.
- 970 Sirota, I., Enzel, Y., & Lensky, N. G. (2017). Temperature seasonality control on modern halite layers
971 in the Dead Sea: In situ observations. *Bulletin*, 129(9-10), 1181-1194. <https://doi.org/10.1130/B31661.1>
- 972 Sittler, C. (1965). Le Paléogène des fossés rhénan et rhodanien. Etudes sédimentologiques et
973 paléoclimatiques. *Mém. Serv. Carte Géol. Alsace Lorrain*, 24, 392 p.
- 974 Straume, E. O., Nummelin, A., Gaina, C., & Nisancioglu, K. H. (2022). Climate transition at the Eocene–
975 Oligocene influenced by bathymetric changes to the Atlantic–Arctic oceanic gateways. *Proceedings of*
976 *the National Academy of Sciences*, 119(17). <https://doi.org/10.1073/pnas.2115346119>
- 977 Sturm, M. (1979). Origin and composition of clastic varves. In *Moraines and varves; origin, genesis,*
978 *classification*, Proceedings of an INQUA symposium on genesis and lithology of Quaternary deposits,
979 281-285.
- 980 Taner, M. T. (2000). *Attributes Revisited*, Technical Publication. Rock Solid Images, Inc., Houston,
981 Texas.
- 982 Tanner, L. H. (2010). Continental carbonates as indicators of paleoclimate. *Developments in*
983 *Sedimentology*, 62, 179-214. [https://doi.org/10.1016/S0070-4571\(09\)06204-9](https://doi.org/10.1016/S0070-4571(09)06204-9)
- 984 Tardif, D., Toumoulin, A., Fluteau, F., Donnadiou, Y., Le Hir, G., Barbolini, N., Licht, A., Ladant, J. B.,
985 Sepulchre, P., Viovy, N., Hoon, C., & Dupont-Nivet, G. (2021). Orbital variations as a major driver of
986 climate and biome distribution during the greenhouse to icehouse transition. *Science Advances*, 7(43).
987 <https://doi.org/10.1126/sciadv.abh2819>
- 988 Thomson, D. J. (1982). Spectrum estimation and harmonic analysis. *Proceedings of the IEEE*, 70(9),
989 1055-1096. <https://doi.org/10.1109/PROC.1982.12433>
- 990 Toumoulin, A., Donnadiou, Y., Ladant, J. B., Batenburg, S. J., Poblete, F., & Dupont-Nivet, G. (2020).
991 Quantifying the Effect of the Drake Passage Opening on the Eocene Ocean. *Paleoceanography and*
992 *Paleoclimatology*, 35(8), e2020PA003889. <https://doi.org/10.1029/2020PA003889>
- 993 Toumoulin, A., Tardif, D., Donnadiou, Y., Licht, A., Ladant, J. B., Kunzmann, L., & Dupont-Nivet, G.
994 (2022). Evolution of continental temperature seasonality from the Eocene greenhouse to the Oligocene
995 icehouse—a model–data comparison. *Climate of the Past*, 18(2), 341-362. <https://doi.org/10.5194/cp-18-341-2022>
996

- 997 Tramoy, R., Salpin, M., Schnyder, J., Person, A., Sebilo, M., Yans, J., Vaury, V., Fozzani, J., & Bauer,
998 H. (2016). Stepwise palaeoclimate change across the Eocene–Oligocene transition recorded in
999 continental NW Europe by mineralogical assemblages and $\delta^{15}\text{N}_{\text{org}}$ (Rennes Basin, France). *Terra*
1000 *Nova*, 28(3), 212-220. <https://doi.org/10.1111/ter.12212>
- 1001 Utescher, T., Bondarenko, O. V., & Mosbrugger, V. (2015). The Cenozoic Cooling–continental signals
1002 from the Atlantic and Pacific side of Eurasia. *Earth and Planetary Science Letters*, 415, 121-133.
1003 <https://doi.org/10.1016/j.epsl.2015.01.019>
- 1004 Warren, J. K. (2016). *Evaporites: A geological compendium*. Springer. [https://doi.org/10.1007/978-3-](https://doi.org/10.1007/978-3-319-13512-0)
1005 [319-13512-0](https://doi.org/10.1007/978-3-319-13512-0)
- 1006 Weedon, G. P. (2003). *Time Series Analysis and Cyclostratigraphy: Examining Stratigraphic Records*
1007 *of Environmental Cycles*. Cambridge University Press. <https://doi.org/10.1017/CBO9780511535482>
- 1008 Weltje, G. J., Bloemsa, M. R., Tjallingii, R., Heslop, D., Röhl, U., & Croudace, I. W. (2015). Prediction
1009 of geochemical composition from XRF core scanner data: a new multivariate approach including
1010 automatic selection of calibration samples and quantification of uncertainties. *Micro-XRF Studies of*
1011 *Sediment Cores: Applications of a non-destructive tool for the environmental sciences*, 507-534.
1012 https://doi.org/10.1007/978-94-017-9849-5_21
- 1013 Westerhold, T., Marwan, N., Drury, A. J., Liebrand, D., Agnini, C., Anagnostou, E., Barnet, J. S. K.,
1014 Bohaty, S. M., De Vleeschouwer, D., Florindo, F., Frederichs, T., Hodell, D. A., Holbourn, A. E., Kroon,
1015 D., Laurentano, V., Littler, K., Lourens, L. J., Lyle, M., Pälike, H., Röhl, U., Tian, J., Wilkens, R. H., Wilson,
1016 P. A., & Zachos, J. C. (2020). An astronomically dated record of Earth's climate and its predictability
1017 over the last 66 million years. *Science*, 369(6509), 1383-1387. <https://doi.org/10.1126/science.aba6853>
- 1018 Wilson, M. V., & Bogen, A. (1994). Tests of the annual hypothesis and temporal calibration of a 6375-
1019 varve fish-bearing interval, Eocene horsefly beds, British Columbia, Canada. *Historical Biology*, 7(4),
1020 325-339. <https://doi.org/10.1080/10292389409380463>
- 1021 Zachos, J., Pagani, M., Sloan, L., Thomas, E., & Billups, K. (2001). Trends, rhythms, and aberrations
1022 in global climate 65 Ma to present. *science*, 292(5517), 686-693.
1023 <https://doi.org/10.1126/science.1059412>
- 1024 Zanazzi, A., Judd, E., Fletcher, A., Bryant, H., & Kohn, M. J. (2015). Eocene–Oligocene latitudinal
1025 climate gradients in North America inferred from stable isotope ratios in perissodactyl tooth enamel.
1026 *Palaeogeography, Palaeoclimatology, Palaeoecology*, 417, 561-568.
1027 <https://doi.org/10.1016/j.palaeo.2014.10.024>
- 1028 Zolitschka, B., Francus, P., Ojala, A. E., & Schimmelmann, A. (2015). Varves in lake sediments—a
1029 review. *Quaternary Science Reviews*, 117, 1-41. <https://doi.org/10.1016/j.quascirev.2015.03.019>